Defect extremal surfaces for entanglement negativity

Debarshi Basu,[*] Himanshu Parihar,[†] Vinayak Raj,[‡] and Gautam Sengupta[§]
Department of Physics, Indian Institute of Technology, Kanpur 208 016, India

(Received 7 November 2022; accepted 29 September 2023; published 7 November 2023)

We propose a doubly holographic version of the semiclassical island formula for the entanglement negativity in the framework of the defect AdS/BCFT correspondence where the anti–de Sitter (AdS) bulk contains a defect conformal matter theory. In this context, we propose a defect extremal surface (DES) formula for computing the entanglement negativity modified by the contribution from the defect matter theory on the end-of-the-world brane. The equivalence of the DES proposal and the semiclassical island formula for the entanglement negativity is demonstrated in $\mathrm{AdS}_3/\mathrm{BCFT}_2$ framework. Furthermore, in the time-dependent $\mathrm{AdS}_3/\mathrm{BCFT}_2$ scenarios involving eternal black holes in the lower dimensional effective description, we investigate the time evolution of the entanglement negativity through the DES and the island formulas and obtain the analogs of the Page curves.

DOI: 10.1103/PhysRevD.108.106005

I. INTRODUCTION

From the past few decades, the study of the black hole information loss paradox has led to several key insights about semiclassical and quantum gravity. Recently, tremendous progress has been made towards a possible resolution of this paradox which involves the appearance of regions termed *"islands"* in the black hole geometry at late times [1–6]. This leads to the Page curve [7–9], which indicates that the process of black hole formation and evaporation follows a unitary evolution. The appearance of the islands stems from the late time dominance of the *replica wormhole* saddles in the gravitational path integral for the Rényi entanglement entropy. The resultant island formula was inspired by the advent of quantum extremal surfaces (QES) introduced earlier, to compute the quantum corrections to the holographic entanglement entropy [10–13]. In this connection, in [1,3,5,6] a quantum dot [e.g. the Sachdev-Ye-Kitaev (SYK) model] coupled to a CFT_2 on a half line was regarded as the holographic dual to a 2-dimensional conformal field theory (CFT) coupled to semiclassical gravity on a hybrid manifold.[1] For such 2-dimensional conformal field theories coupled to semiclassical gravity, the island formula involves the fine-grained entropy of the Hawking radiation in a region R, obtained through the extremization over the entanglement entropy island region $I(R)$ and is expressed as follows:

$$S[R] = \min \operatorname*{ext}_{I(R)}\left[\frac{\mathrm{Area}[\partial I(R)]}{4G_N} + S_{\mathrm{eff}}(R\cup I(R))\right], \qquad (1.1)$$

where G_N is the Newton's constant and $S_{\mathrm{eff}}(X)$ corresponds to the effective semiclassical entanglement entropy of quantum matter fields located on X. For recent related works, see Refs. [14–121].

A natural description for the island formulation was provided through a *double-holographic* framework [1] where the d-dimensional conformal field theory coupled to semiclassical gravity may be interpreted as a lower-dimensional effective description of a bulk $(d+1)$-dimensional theory of gravity. In this scenario, the d-dimensional conformal field theory is considered to possess a dual bulk $(d+1)$-dimensional gravitational theory in the $\mathrm{AdS}_{d+1}/\mathrm{CFT}_d$ framework. In the double holographic picture the computation of the entanglement entropy through the island formula in the lower-dimensional theory reduces to its holographic characterization through the Ryu-Takayanagi (RT) formula [10,11] in the bulk dual AdS_{d+1} geometry. This may be understood as a realization of the $\mathrm{ER}=\mathrm{EPR}$ proposal [122] where the island region in the black hole interior is contained within the entanglement wedge of the radiation bath through the double-holographic perspective.

On a separate note, CFT_2s on a manifold with a boundary, termed as boundary conformal field theories (BCFT_2s) [123] have received considerable attention in the recent past. The holographic dual of such BCFT_2s [124–128]

[*]debarshi@iitk.ac.in
[†]himansp@iitk.ac.in
[‡]vraj@iitk.ac.in
[§]sengupta@iitk.ac.in

[1]In such holographic dual theories, the hybrid manifold on which the CFT is defined consists of a flat bath along with a curved geometry with dynamical gravity.

involves an asymptotically AdS_3 spacetime truncated by an end-of-the-world (EOW) brane $\mathbb{Q}$ with Neumann boundary condition. An extension of this $\mathrm{AdS}_3/\mathrm{BCFT}_2$ duality studied in [45], involved additional *defect* conformal matter on the EOW brane $\mathbb{Q}$ which resulted in the modification of the Neumann boundary condition. The entanglement entropy of an interval in this defect BCFT_2 was also computed in [45,94] through a modification of the quantum corrected RT formula. This was termed as the defect extremal surface (DES) formula as it involved contributions from the defect conformal matter fields. Interestingly, this DES formula has been proposed to be the doubly holographic counterpart of the island formula in the context of the defect $\mathrm{AdS}_3/\mathrm{BCFT}_2$ scenario [45]. The authors in [45] compared the entanglement entropy computed through the DES formula in the $3d$ bulk geometry with that computed through the island formula in the effective $2d$ description and found an exact agreement. Subsequently, the time dependent $\mathrm{AdS}_3/\mathrm{BCFT}_2$ scenario was studied in [94], where in the effective $2d$ description, an eternal black hole emerges on the EOW brane. The entanglement entropy for the Hawking radiation from the eternal black hole, obtained through the DES formula reproduced the Page curve and was consistent with the island proposal.

The fine grained entanglement entropy is a viable measure of entanglement for bipartite pure states. For configurations involving bipartite pure states in black hole geometries, the island proposal in the effective picture or the DES formula in the doubly holographic scenario correctly encode the entanglement structure of the Hawking radiation. However, entanglement entropy fails to characterize the structure of entanglement for bipartite mixed states as it receives contributions from irrelevant classical and quantum correlations. For such cases involving bipartite mixed states, it is required to consider alternative mixed-state correlation or entanglement measures. Several of such correlation and entanglement measures like the reflected entropy [129,130], the entanglement negativity [131,132], the entanglement of purification [133,134] and the balanced partial entanglement entropy [135,136] have been studied in the literature.

In this context, the crucial issue of characterization of the entanglement structure of bipartite mixed states was addressed in [63] through the computation of the reflected entropy in the time dependent framework involving an eternal black hole in the $\mathrm{AdS}_3/\mathrm{BCFT}_2$ scenario. The authors proposed a $3d$ bulk DES formula for the reflected entropy and compared their results with the $2d$ effective field theory computations involving islands. They obtained the analogs of the Page curves for the reflected entropy and demonstrated the appearance of islands at late times.

The above developments bring into sharp focus the crucial issue of the characterization of the mixed-state entanglement structure of the Hawking radiation from black holes. In this context, the nonconvex entanglement monotone termed the *entanglement negativity* [131,132] serves as a natural candidate to investigate the entanglement structure of such mixed states. The entanglement negativity has been explored in conformal field theories [137–139] through appropriate replica techniques.[2] Subsequently several holographic constructions for computing the entanglement negativity in the context of the AdS/CFT correspondence was advanced in a series of interesting works[3] in [143–156] which reproduced the field theoretic results in the large central-charge limit [141,157,158]. Interestingly, in [159–163], an alternative holographic proposal based on the bulk entanglement wedge cross section (EWCS) was also investigated. In this connection, an island formulation for the entanglement negativity was recently established in [164] following a similar island construction for the reflected entropy developed in [26,27].[4] Furthermore, a geometric construction based on the double holographic framework was discussed qualitatively in [164] and subsequently investigated in [165] through a partial dimensional reduction [103] of the $3d$ bulk space time. In this article, we generalize these doubly holographic scenarios to the framework of AdS/BCFT with defect conformal matter on the EOW brane. We propose a DES formula for computing the bulk entanglement negativity in asymptotically AdS_3 geometries truncated by an EOW brane. Furthermore, we demonstrate the equivalence of the DES results with the corresponding island computations for the entanglement negativity of bipartite mixed states in both static and time-dependent configurations involving black hole/bath systems in the effective lower dimensional theory.

The rest of the article is organized as follows. In Sec. II, we recollect various aspects of the DES formula for the entanglement entropy and the corresponding effective lower dimensional picture involving the entanglement islands. In Sec. III, we provide the island construction for the entanglement negativity [164], and propose the DES formulas for computing the bulk entanglement negativity for disjoint and adjacent subsystems on the conformal boundary of asymptotically AdS_3 geometries with defect conformal matter on the EOW brane. In Sec. IV, we compute the entanglement negativity for disjoint and adjacent intervals in a static time slice of the conformal boundary. Beginning with a brief review of the eternal black hole configuration in the $2d$ effective semiclassical picture, we describe DES and island computations for the entanglement negativity between interior regions of the

[2] For an extension of this replica technique in the Galilean conformal field theories, see Ref. [140].

[3] For analogs of these proposals in the context of flat holography, see Refs. [141,142].

[4] Note that, [164] also provided an alternative island formulation for the entanglement negativity which generalizes the proposals in [159–163] in terms of the generalized Rényi reflected entropy of order one half.

black hole, between the black hole and radiation in the bath region, and between radiation segments, and demonstrate the equivalence of the two formulations in Sec. V. In Sec. VI, we summarize our results and comment on possible future directions. Additionally, in Appendix, we have obtained the entanglement negativity in the effective semiclassical description utilizing the alternative island proposal (cf. footnote 4) advanced in [164] for certain bipartite configurations in the static AdS/BCFT model.

II. REVIEW OF EARLIER LITERATURE

In this section, we will briefly recall the salient features of the holographic model under consideration. We first review the AdS/BCFT scenario [124] modified through the inclusion of conformal matter on the end-of-the-world (EOW) brane which was proposed in [45,94]. Following this, we describe the defect extremal surface formula [45] for computing the entanglement entropy in the bulk AdS geometry truncated by the EOW brane. We will also briefly elucidate the effective $2d$ description of the model and the semiclassical island formula for computing the entanglement entropy of a subsystem in the effective description.

A. $AdS_3/BCFT_2$

As described in [124,125] the bulk dual of a $BCFT_2$ defined on the half line $x \geq 0$ is given by an AdS_3 geometry truncated by an EOW brane $\mathbb{Q}$ with Neumann boundary conditions. The gravitational action of the bulk manifold $\mathcal{N}$ is given by

$$I = \int_{\mathcal{N}} \sqrt{-g}(R - 2\Lambda) + 2\int_{\mathbb{Q}} \sqrt{-h}(K - T), \qquad (2.1)$$

where h_{ab} is the induced metric, K is the trace of the extrinsic curvature K_{ab} on the EOW brane $\mathbb{Q}$ with a tension T. The Neumann boundary condition on the EOW brane is given as $K_{ab} = (K - T)h_{ab}$. The $3d$ bulk geometry may be described by two sets of relevant coordinate charts, (t, x, z) and (t, ρ, y), which are related through

$$x = y \tanh\left(\frac{\rho}{\ell}\right), \qquad z = -y \,\mathrm{sech}\left(\frac{\rho}{\ell}\right). \qquad (2.2)$$

The bulk metric in these coordinates is given by the standard Poincaré slicing, as follows:

$$\begin{aligned} ds^2 &= d\rho^2 + \cosh^2\left(\frac{\rho}{\ell}\right)\frac{-dt^2 + dy^2}{y^2} \\ &= \frac{\ell^2}{z^2}(-dt^2 + dx^2 + dz^2), \end{aligned} \qquad (2.3)$$

where ℓ is the AdS_3 radius. In the Poincaré slicing[5] described by the (t, ρ, y) coordinate chart the EOW brane is situated at a constant $\rho = \rho_0$ slice and the induced metric on the brane is given by that of an AdS_2 geometry [124].

An extension to this usual $AdS_3/BCFT_2$ framework was proposed in [45] where one essentially begins with an orthogonal brane with zero tension and through the addition of conformal matter onto it, turns on a finite tension. The Neumann boundary condition on the EOW brane $\mathbb{Q}$ is modified by the stress tensor of this defect CFT_2. The EOW brane $\mathbb{Q}$ is then treated as a defect in the bulk geometry.

B. Defect extremal surface

For the modified bulk picture with defect conformal matter on $\mathbb{Q}$, the entanglement entropy of an interval A in the original $BCFT_2$ involves contributions from the defect matter, and the usual RT formula [10] is modified to the DES formula [45,94] given as

$$\begin{aligned} S_{\mathrm{DES}}(A) &= \min_{\Gamma_A, X} \mathrm{ext}\left[\frac{\mathcal{A}(\Gamma_A)}{4G_N} + S_{\mathrm{defect}}(D)\right], \\ X &= \Gamma_A \cap D, \end{aligned} \qquad (2.4)$$

where Γ_A is a codimension two extremal surface homologous to the subsystem A and D is the defect region along the EOW brane $\mathbb{Q}$ as depicted in Fig. 1.

For an interval $A = [0, L]$ in the $BCFT_2$, the generalized entanglement entropy corresponding to a defect $D = [-a, 0]$ on the brane CFT_2 may be computed through the DES formula as follows[6] [45]:

$$\begin{aligned} S_{\mathrm{gen}}(a) &= \frac{\mathcal{A}(\Gamma_A)}{4G_N} + S_{\mathrm{defect}}([-a, 0]) \\ &= \frac{\ell}{4G_N}\cosh^{-1}\left[\frac{(L + a\sin\theta_0)^2 + (a\cos\theta_0)^2}{2\epsilon\, a\cos\theta_0}\right] \\ &\quad + \frac{c}{6}\log\left(\frac{2\ell}{\epsilon_y \cos\theta_0}\right), \end{aligned} \qquad (2.5)$$

Note that the defect contribution to the generalized entropy is a constant which implies that the defect extremal surface is same as the RT surface for the subsystem A. Extremization with respect to the position a of the defect leads to the entanglement entropy of the subsystem A as follows:

[5]A convenient choice for a polar coordinate is $\theta = \arccos[\mathrm{sech}(\frac{\rho}{\ell})]$, which determines the angular position of the brane from the vertical as shown in Fig. 1.

[6]Note that we are using the standard geodesic length formula for Poincaré AdS_3 instead of the AdS/BCFT techniques employed in [45,94] as both the procedures lead to the same answer and are therefore complementary.

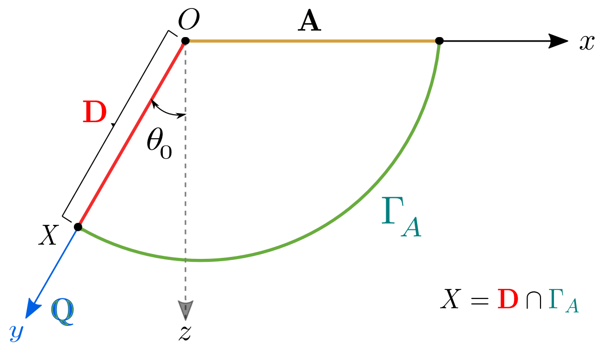

FIG. 1. Schematics of the defect extremal surface for the entanglement entropy of a subsystem A. Figure modified from [45].

$$S_{\mathrm{DES}}([0,L]) = \frac{c}{6}\left[\log\left(\frac{2L}{\epsilon}\right) + \tanh^{-1}(\sin\theta_0) + \log\left(\frac{2\ell}{\epsilon_y\cos\theta_0}\right)\right], \tag{2.6}$$

where both the central charges of the original BCFT and the defect CFT_2 are taken to be equal[7] to c.

We would like to note that the model discussed in this article differs from the typical Karch-Randall (KR) models. In the usual KR braneworld models, the EOW brane has a high tension and is therefore pushed towards the asymptotic boundary of the bulk spacetime, causing the AdS isometries on the brane to act as conformal transformations [35,36,51]. For such cases, the brane contains a copy of the same CFT (defined by the Polyakov action for the gravity theory on the brane) as that on the asymptotic boundary. In the present work, we have instead maintained the EOW brane at a finite tension, and as a result, it has no inherent CFT. The defect conformal matter has been incorporated on the EOW brane, to provide a $2d$ perspective consistent with the QES formulation. Subsequently, the effective $2d$ braneworld description is achieved by combining a partial Randall-Sundrum reduction and the typical AdS/BCFT duality [45], which leads to a BCFT on a half line coupled to a dynamical EOW brane containing defect matter.

C. Effective description and boundary island formula

The lower-dimensional effective semiclassical theory for the bulk configuration described above may be obtained through a combination of a partial Randall-Sundrum reduction [166,167] and the usual AdS/BCFT duality [168]. As described in [45,63,94], this is implemented by dividing the AdS_3 bulk into two parts through the insertion of an imaginary codimension one surface $\mathbb{Q}'$ orthogonal to the asymptotic boundary, with transparent boundary conditions. The portion of the bulk enclosed between $\mathbb{Q}$ and $\mathbb{Q}'$ is dimensionally reduced along the ρ direction using a partial Randall-Sundrum reduction thereby obtaining a effective $2d$ gravitational theory coupled with the matter CFT_2 on $\mathbb{Q}$. On the other hand, the rest of the bulk is dual to the original BCFT_2 on the half line $x \geq 0$ from the usual AdS/BCFT duality. The transparent boundary conditions along $\mathbb{Q}'$ naturally glues the gravity theory on $\mathbb{Q}$ and the BCFT_2 on the half line $x \geq 0$, leading to an effective $2d$ semiclassical theory on a hybrid manifold, similar to that considered in [1,3].

In the effective semiclassical description described above, one may utilize the island formula [1,3] to compute the entanglement entropy. For a subsystem $A = [0, L]$ in the flat CFT_2 on the asymptotic boundary, an island region $I_A = [-a, 0]$ appears in the gravitational sector on the EOW brane $\mathbb{Q}$. The entanglement entropy is obtained by extremizing the generalized entropy functional as

$$\begin{aligned} S_{\mathrm{bdy}} &= \operatorname*{ext}_a S_{\mathrm{gen}}(a) = \operatorname*{ext}_a[\mathcal{A}(y=-a) + S_{\mathrm{matter}}([-a, L])] \\ &= \frac{c}{6}\tanh^{-1}(\sin\theta_0) + \frac{c}{6}\log\left(\frac{4L\ell}{\epsilon\,\epsilon_y\cos\theta_0}\right). \end{aligned} \tag{2.7}$$

The first term in the above expression is due to the constant area of the quantum extremal surface in the $\mathrm{AdS}_3/\mathrm{BCFT}_2$ framework, given as [45]

$$\mathcal{A}(\partial I_A) \equiv \frac{\rho_0}{4G_N} = \frac{\ell}{4G_N}\tanh^{-1}(\sin\theta_0), \tag{2.8}$$

where θ_0 is the angle of the EOW brane with the vertical. It is observed from the above that the island formula leads to the same expression for the entanglement entropy as the DES result in Eq. (2.6). In other words, the DES formula may be considered as the doubly holographic counterpart of the island formula in the defect AdS/BCFT framework.

D. Entanglement negativity

In this subsection, we will briefly review the salient features of the mixed-state entanglement measure termed the entanglement negativity and its holographic characterization in the context of $\mathrm{AdS}_3/\mathrm{CFT}_2$ scenario. In a seminal work [131], Vidal and Werner introduced the computable mixed-state entanglement measure, the entanglement negativity which is defined as the trace norm of the density matrix partially transposed with respect to one of the subsystems. In [137–139], replica techniques were developed to obtain the entanglement negativity for subsystems in CFT_2 s which involved the even parity n_e of the replica

[7]Note that the equality of the two central charges is essential to relate the present bulk description to the effective $2d$ island scenario which involves a single CFT_2 on the complete hybrid manifold. On the other hand, for different central charges of the BCFT on the asymptotic boundary and the defect CFT_2 on the brane, a generalization of the island formula will be required even when two interacting CFTs are considered.

index. The entanglement negativity was obtained through the analytic continuation of the replica index $n_e \to 1$ as follows:

$$\mathcal{E} = \lim_{n_e \to 1} \log \mathrm{Tr}(\rho_{AB}^{T_B})^{n_e}, \tag{2.9}$$

where the superscript T_B denotes partial transposition with respect to the subsystem B. The trace $\mathrm{Tr}(\rho_{AB}^{T_B})^{n_e}$ may be expressed as a twist-field correlator in the CFT_2, corresponding to the bipartite state under consideration. As an example, we consider the generic bipartite mixed state of two disjoint intervals $A = [u_1, v_1]$ and $B = [u_2, v_2]$ in a CFT_2. The trace $\mathrm{Tr}(\rho_{AB}^{T_B})^{n_e}$ is then given by the following four-point correlator of *twist fields*,

$$\begin{aligned}&\mathrm{Tr}(\rho_{AB}^{T_B})^{n_e}\\&\quad = \langle \mathcal{T}_{n_e}(u_1)\bar{\mathcal{T}}_{n_e}(v_1)\bar{\mathcal{T}}_{n_e}(u_2)\mathcal{T}_{n_e}(v_2)\rangle_{\mathrm{CFT}^{\otimes n_e}},\end{aligned} \tag{2.10}$$

where the twist fields $\mathcal{T}_{n_e}$ and $\bar{\mathcal{T}}_{n_e}$ are primary fields with conformal dimensions

$$\Delta_{n_e} = \frac{c}{12}\left(n_e - \frac{1}{n_e}\right). \tag{2.11}$$

Subsequently, in a series of works [144–146,151], several holographic proposals for the entanglement negativity were proposed for specific bipartite mixed states. These proposals involved appropriate algebraic sums of the lengths of codimension two bulk-static minimal surfaces homologous to various subsystems describing the mixed state. In particular, for two disjoint intervals A and B sandwiching another interval C in a CFT_2, the holographic entanglement negativity may be obtained geometrically in the context of the $\mathrm{AdS}_3/\mathrm{CFT}_2$ correspondence as follows [151]:

$$\mathcal{E}(A:B) = \frac{3}{16G_N}(\mathcal{L}_{AC} + \mathcal{L}_{BC} - \mathcal{L}_C - \mathcal{L}_{ABC}), \tag{2.12}$$

where $\mathcal{L}_X$ denotes the length of the extremal curve homologous to subsystem X. The configuration of two adjacent intervals A and B may be obtained through the limit $C \to \varnothing$ of the above, and the holographic entanglement negativity is given as [146]

$$\mathcal{E}(A:B) = \frac{3}{16G_N}(\mathcal{L}_A + \mathcal{L}_B - \mathcal{L}_{AB}). \tag{2.13}$$

Note that, these proposals have further been extended to various other holographic frameworks including flat holography [141], anomalous AdS/CFT [156] as well as higher-dimensional scenarios [147,153–155].

We would also like to mention here that an alternative holographic proposal for entanglement negativity was forwarded by the authors of [159] based on the bulk entanglement wedge cross section. This proposal was further refined and was stated in terms of the Rényi reflected entropy as follows [160]:

$$\tilde{\mathcal{E}}(A:B) = \frac{1}{2}S_R^{(1/2)}(A:B). \tag{2.14}$$

For the special class of subsystems in holographic CFT_ds involving spherical entangling surfaces, the backreaction on the geometry is accounted for by a dimension dependent constant $\mathcal{X}_d$, which for a 3-dimensional bulk is given by $\mathcal{X}_2 = \frac{3}{2}$.

On a related note, the authors in [169] established an inequality between the reflected entropy and the mutual information in terms of the fidelity of a Markov recovery process related to the purification of the mixed state under consideration. This difference between the reflected entropy and the mutual information was termed as the Markov gap which turned out to be constant at the leading order. It was geometrically shown to be described in terms of the numbers of nontrivial boundaries[8] of the EWCS. In several earlier works [145,146,151], the holographic entanglement negativity has also been related to the holographic mutual information which implies that the above alternative proposal for the holographic entanglement negativity in terms of the Rényi reflected entropy should also be modified to incorporate this Markov gap.

III. DEFECT EXTREMAL SURFACE FOR ENTANGLEMENT NEGATIVITY

In this section, we propose the defect extremal surface formula for the entanglement negativity in the AdS/BCFT models which include defect conformal matter on the EOW brane [45,63,94]. To begin with, we recall the semiclassical QES formula for the entanglement negativity involving entanglement islands in the lower-dimensional effective picture discussed earlier. As described in [164,165], the QES proposal for the entanglement negativity between two disjoint intervals in the effective boundary description is given by[9,10]

$$\begin{aligned}&\mathcal{E}^{\mathrm{bdy}}(A:B)\\&\quad = \min \underset{\Gamma = \partial I_A \cap \partial I_B}{\mathrm{ext}}\left[\frac{3}{16G_N}(\mathcal{A}(\partial I_A) + \mathcal{A}(\partial I_B) - \mathcal{A}(\partial I_{AB}))\right.\\&\qquad \left. + \mathcal{E}^{\mathrm{eff}}(A \cup I_A :\ B \cup I_B)\right],\end{aligned} \tag{3.1}$$

[8]Note that trivial boundaries of the bulk EWCS are those which end on the boundary of the spacetime [169].

[9]Note that, in this article, we use the nomenclature *boundary description* and *lower-dimensional effective description* interchangeably.

[10]See Appendix for discussion about the island prescription for entanglement negativity through the alternative proposal described in Eq. (2.14).

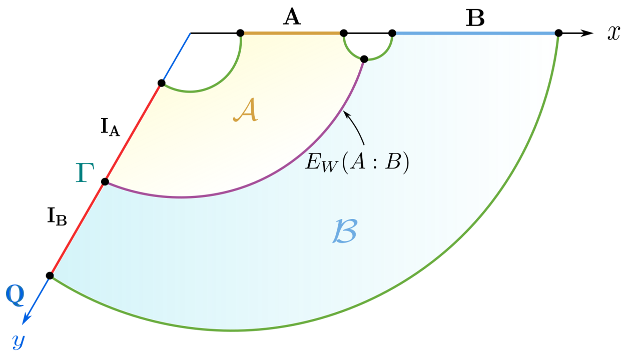

FIG. 2. Schematics of the quantum extremal surface for the entanglement negativity between two disjoint intervals A and B, where I_A and I_B are the entanglement negativity islands satisfying the constraint $I_A \cup I_B = I(A \cup B)$. The island cross section is given by $\Gamma \equiv \partial I_A \cap \partial I_B$. In the double holographic picture described in [164], the $3d$ bulk entanglement wedge cross section ending at the point Γ on the EOW brane $\mathbb{Q}$ splits the entanglement wedge corresponding to $A \cup B$ into two parts $\mathcal{A}$ and $\mathcal{B}$. Figure modified from [63].

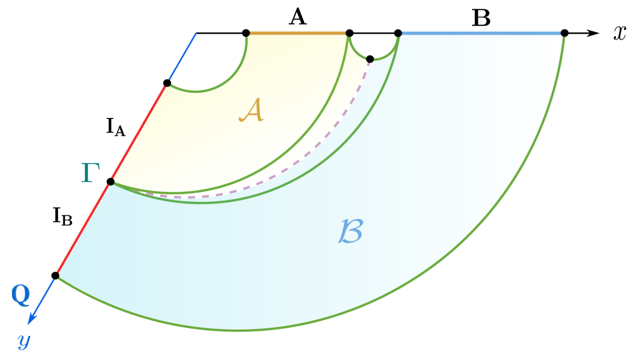

FIG. 3. Schematics of the defect extremal surfaces for the entanglement negativity between two disjoint intervals A and B. I_A and I_B denote the entanglement negativity islands corresponding to A and B, respectively. The interval C sandwiched between A and B does not have an island.

where I_A and I_B are the entanglement negativity islands corresponding to subsystems A and B, respectively. The entanglement negativity islands obeys the condition $I_A \cup I_B = I(A \cup B)$, where $I(A \cup B)$ denotes the entanglement entropy island for $A \cup B$, as illustrated in Fig. 2. Furthermore, the extremization in the QES formula is performed over the location of the *island cross section* $\Gamma \equiv \partial I_A \cap \partial I_B$. In this context, utilizing the constraint $I_A \cup I_B = I(A \cup B)$, the algebraic sum of the area contributions in Eq. (3.1) may be reduced to that corresponding to the island cross section Γ. Hence, the QES formula may be expressed as [164]

$$\mathcal{E}^{\mathrm{bdy}}(A:B) = \min_{\Gamma} \mathrm{Ext}\left[\frac{3}{8G_N}\mathcal{A}(\Gamma = \partial I_A \cap \partial I_B) + \mathcal{E}^{\mathrm{eff}}(A \cup I_A :\, B \cup I_B)\right]. \tag{3.2}$$

Inspired by the holographic characterizations for the entanglement negativity described earlier, we now propose DES formulas to obtain the entanglement negativity in the doubly holographic framework of the defect $\mathrm{AdS_3/BCFT_2}$ scenario. In the presence of the bulk defect theory, the entanglement negativity for a bipartite mixed state ρ_{AB} in the dual $\mathrm{BCFT_2}$ involves corrections from the bulk matter fields. Following [12,13], the effective matter contribution is given by the bulk entanglement negativity between the regions $\mathcal{A}$ and $\mathcal{B}$ which are obtained by splitting the codimension one region dual to ρ_{AB} via the entanglement wedge cross section.[11] For the bipartite mixed-state configuration described by two disjoint intervals A and B in the dual $\mathrm{CFT_2}$, the $3d$ bulk dual DES formula for the entanglement negativity is therefore given by

$$\mathcal{E}^{\mathrm{bulk}}(\mathcal{A}:\mathcal{B}) = \min_{\Gamma} \mathrm{Ext}\left[\frac{3}{16G_N}(\mathcal{L}(\gamma_{AC}) + \mathcal{L}(\gamma_{BC}) - \mathcal{L}(\gamma_C) - \mathcal{L}(\gamma_{ABC})) + \mathcal{E}^{\mathrm{eff}}(\mathcal{A}:\mathcal{B})\right], \tag{3.3}$$

where $\mathcal{L}(\gamma_X)$ is the length of the bulk extremal curve homologous to the interval X on the boundary $\mathrm{CFT_2}$ as illustrated in Fig. 3 and $\mathcal{E}^{\mathrm{eff}}(\mathcal{A}:\mathcal{B})$ denotes the effective entanglement negativity between the quantum matter fields inside the bulk regions $\mathcal{A}$ and $\mathcal{B}$. The bulk effective term in Eq. (3.3) reduces to the effective entanglement negativity between the entanglement negativity islands I_A and I_B on the EOW brane as the conformal matter is present only on the EOW brane.[12] Note that if the intervals are far away such that their entanglement wedges are disconnected, the contributions coming from the combination of bulk extremal curves vanishes identically due to phase transitions to other entropy saddles [152].

The DES formula for two adjacent intervals A and B in the bulk description may be obtained from Eq. (3.3) through the limit $C \to \varnothing$ as follows:

$$\mathcal{E}^{\mathrm{bulk}}(\mathcal{A}:\mathcal{B}) = \min_{\Gamma} \mathrm{Ext}\left[\frac{3}{16G_N}(\mathcal{L}(\gamma_A) + \mathcal{L}(\gamma_B) - \mathcal{L}(\gamma_{AB})) + \mathcal{E}^{\mathrm{eff}}(\mathcal{A}:\mathcal{B})\right]. \tag{3.4}$$

[11]Note that a defect extremal surface formula for the reflected entropy was developed in [63] utilizing a similar construction. Furthermore, the authors in [63] demonstrated the equivalence of the DES and QES formulas for the reflected entropy in the framework of defect $\mathrm{AdS_3/BCFT_2}$.

[12]Note that due to the localization of the quantum matter only on the EOW brane for the present scenario of defect $\mathrm{AdS_3/BCFT_2}$, the choice of the bulk regions $\mathcal{A}$ and $\mathcal{B}$ is not unique. However any difference with the present proposal is only expected to be observed at the subleading order in c. See also the discussion in Sec. VI.

In the following we will compute the entanglement negativity for various bipartite mixed states in a defect BCFT_2 through the island and the DES formulas and find exact agreement between the bulk and the boundary results.

IV. ENTANGLEMENT NEGATIVITY ON A FIXED TIME SLICE

A. Two disjoint intervals

In this subsection we focus on the computation of the entanglement negativity for the bipartite mixed state of two disjoint intervals $A = [b_1, b_2]$ and $B = [b_3, \infty]$ on a static time slice in the defect $\mathrm{AdS}_3/\mathrm{BCFT}_2$ framework. There are three possible phases for the entanglement negativity for this mixed-state configuration based on the subsystem sizes, which we investigate below.

1. Phase-I

Boundary description. In this phase, the interval C separating the two disjoint intervals A and B is large[13] and the interval A is small enough such that it does not possess an entanglement entropy island. Consequently, there is no nontrivial island cross section on the EOW brane as shown in Fig. 4. Hence $\Gamma = \varnothing$, and the area term in the QES formula Eq. (3.2) vanishes, namely $\mathcal{A}(\Gamma) = 0$.

The effective semiclassical entanglement negativity in this phase may be obtained through a correlation function of twist operators located at the endpoints of the intervals as follows:

$$\begin{aligned}
\mathcal{E}^{\mathrm{eff}}(A\!:\!B\cup I_B) &= \lim_{n_e\to1} \log[(\epsilon_y\Omega(-b_3))^{\Delta_{n_e}}\langle \mathcal{T}_{n_e}(b_1)\bar{\mathcal{T}}_{n_e}(b_2)\bar{\mathcal{T}}_{n_e}(b_3)\mathcal{T}_{n_e}(-b_3)\rangle_{\mathrm{CFT}^{\otimes n_e}}] \\
&\approx \lim_{n_e\to1} \log[(\epsilon_y\Omega(-b_3))^{\Delta_{n_e}}\langle \mathcal{T}_{n_e}(b_1)\bar{\mathcal{T}}_{n_e}(b_2)\rangle_{n_e}\langle \bar{\mathcal{T}}_{n_e}(b_3)\mathcal{T}_{n_e}(-b_3)\rangle_{n_e}] \\
&= 0,
\end{aligned} \tag{4.1}$$

where ϵ_y is the UV cutoff on the EOW brane $\mathbb{Q}$ and the warp factor Ω is given by [45]

$$ds^2_{\mathrm{brane}} = \Omega^{-2}(y)ds^2_{\mathrm{flat}}, \qquad \Omega(-b_3) = \left|\frac{b_3\cos\theta_0}{\ell}\right|. \tag{4.2}$$

In the second equality of Eq. (4.1), we have factorized the given four-point function utilizing the corresponding operator product expansion (OPE) channels. Consequently, in this phase the total entanglement negativity for the two disjoint intervals in the boundary description is vanishing.

Bulk description. The dual bulk description for this phase has a disconnected entanglement wedge and hence we have $\Gamma = \varnothing$ similar to the boundary description. Furthermore, as the bulk matter fields are only localized on the EOW brane $\mathbb{Q}$ and A has no corresponding island, the effective entanglement negativity between bulk quantum matter fields also vanishes as follows:

$$\mathcal{E}^{\mathrm{eff}}(\mathcal{A}\!:\!\mathcal{B}) = \mathcal{E}^{\mathrm{eff}}(\varnothing\!:\!I_B) \equiv 0. \tag{4.3}$$

Hence, in the bulk description the holographic entanglement negativity is entirely given by the contribution from the areas of the defect extremal surfaces. The lengths of the bulk DES homologous to various subsystems are given by

$$\begin{aligned}
\mathcal{L}_{AC} &= \mathcal{L}_1 + \mathcal{L}_3, \qquad \mathcal{L}_{BC} = \mathcal{L}_2 + \mathcal{L}_4, \\
\mathcal{L}_C &= \mathcal{L}_2 + \mathcal{L}_3, \qquad \mathcal{L}_{ABC} = \mathcal{L}_1 + \mathcal{L}_4.
\end{aligned} \tag{4.4}$$

Now utilizing the bulk DES formula for the entanglement negativity for two disjoint intervals in Eq. (3.3), we obtain

$$\mathcal{E}^{\mathrm{bulk}}(\mathcal{A}\!:\!\mathcal{B}) = \frac{3}{16G_N}(\mathcal{L}_{AC} + \mathcal{L}_{BC} - \mathcal{L}_C - \mathcal{L}_{ABC}) = 0. \tag{4.5}$$

Therefore, the boundary and bulk description match trivially, leading to a vanishing entanglement negativity in this phase. Disconnected entanglement wedge for this configuration consequently implies a perfect Markov recovery process and a vanishing Markov gap.

2. Phase-II

Boundary description. Next we turn our attention towards the phase where the interval A is small and still does not possess an island, but unlike earlier the interval C sandwiched between A and B is also small and therefore does not lead to an entanglement entropy island as well (cf. footnote 13). Consequently, the entanglement wedge for $A\cup B$ is connected and the boundary of the semi-infinite island region is determined by the endpoint b_1 of the interval A. In this phase, there is no nontrivial island cross section as depicted in Fig. 5 and hence the area term in Eq. (3.2) vanishes identically. On the other hand, the effective semiclassical entanglement negativity is given by

[13] Note that, in this phase the interval C has an entanglement island. In the bulk description, this corresponds to a disconnected entanglement wedge for $A\cup B$.

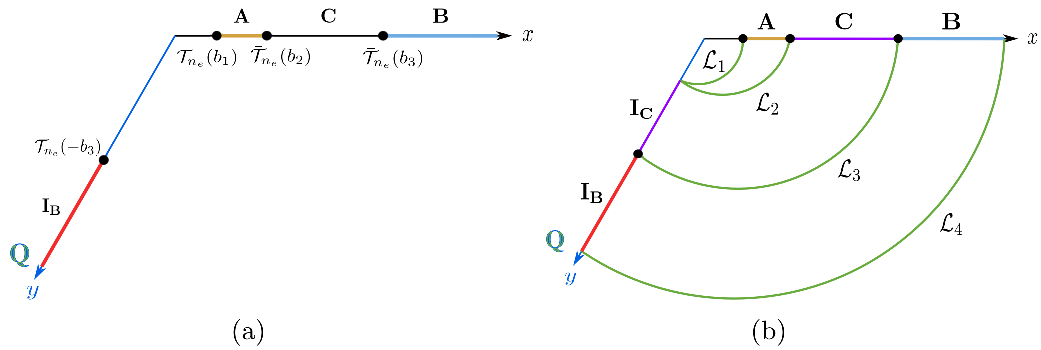

FIG. 4. Schematics of the (a) QES and (b) DES perspective for the defect extremal surface for the entanglement negativity between two disjoint intervals A and B in phase-I.

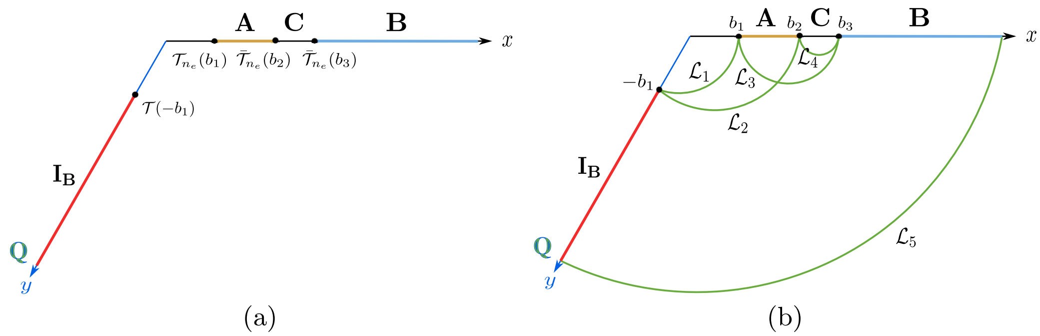

FIG. 5. Schematics of the (a) QES and (b) DES perspective for the defect extremal surface for the entanglement negativity between two disjoint intervals A and B in phase-II.

$$\mathcal{E}^{\mathrm{eff}}(A:B\cup I_B) = \lim_{n_e\to 1} \log[(\epsilon_y\Omega(-b_1))^{\Delta_{n_e}}\langle \mathcal{T}_{n_e}(-b_1)\mathcal{T}_{n_e}(b_1)\bar{\mathcal{T}}_{n_e}(b_2)\bar{\mathcal{T}}_{n_e}(b_3)\rangle_{\mathrm{CFT}^{\otimes n_e}}]. \tag{4.6}$$

As described in [151,152,157], for the t-channel where the intervals A and B are in proximity of each other (cross-ratio $x\to 1$), in the large central-charge limit the above four-point correlation function of the twist operators has the following form:

$$\langle \mathcal{T}_{n_e}(-b_1)\mathcal{T}_{n_e}(b_1)\bar{\mathcal{T}}_{n_e}(b_2)\bar{\mathcal{T}}_{n_e}(b_3)\rangle_{\mathrm{CFT}^{\otimes n_e}} = (1-x)^{\hat{\Delta}}, \tag{4.7}$$

where the conformal dimension $\hat{\Delta}$ corresponding to the dominant Virasoro conformal block, and the cross-ratio x are given as

$$\hat{\Delta} = \frac{c}{6}\left(\frac{n_e}{2}-\frac{2}{n_e}\right), \qquad x = \frac{(b_2-b_1)(b_3+b_1)}{(b_2+b_1)(b_3-b_1)}. \tag{4.8}$$

We may now obtain the entanglement negativity for this phase in the boundary description by substituting Eqs. (4.7) and (4.8) in Eq. (4.6) to be

$$\mathcal{E}^{\mathrm{bdy}}(A:B) = \frac{c}{4}\log\left[\frac{(b_1+b_2)(b_3-b_1)}{2b_1(b_3-b_2)}\right]. \tag{4.9}$$

Bulk description. From the bulk perspective, in this phase the entanglement wedge corresponding to $A\cup B$ is connected. However, as the interval A does not have an island, the minimal entanglement wedge cross section does not meet the EOW brane $\mathbb{Q}$ resulting in a trivial island cross section $\Gamma=\varnothing$. Hence, the effective entanglement negativity between the bulk quantum matter fields vanishes similar to Eq. (4.3). The bulk entanglement negativity consists of the contributions from the combination of the defect extremal surfaces as depicted in Fig. 5(b). Now utilizing Eq. (3.3), we may obtain the entanglement negativity between A and B in this phase as follows:

$$\begin{aligned}\mathcal{E}^{\mathrm{bulk}}(\mathcal{A}:\mathcal{B}) &= \frac{3}{16G_N}[\mathcal{L}_3+(\mathcal{L}_2+\mathcal{L}_5)-\mathcal{L}_4-(\mathcal{L}_1+\mathcal{L}_5)]\\ &= \frac{3}{16G_N}(\mathcal{L}_2+\mathcal{L}_3-\mathcal{L}_1-\mathcal{L}_4).\end{aligned} \tag{4.10}$$

In the framework of defect $\mathrm{AdS}_3/\mathrm{BCFT}_2$ [45,63,94], it was observed that the defect extremal surfaces have the same structure as the corresponding RT surfaces since the contribution from the defect matter fields turned out to be constant. The lengths of the defect extremal surfaces $\mathcal{L}_3$ and $\mathcal{L}_4$ in Eq. (4.10) are given by [10,124]

$$\mathcal{L}_3 = 2\ell \log\left(\frac{b_3 - b_1}{\epsilon}\right), \quad \mathcal{L}_4 = 2\ell \log\left(\frac{b_3 - b_2}{\epsilon}\right), \quad (4.11)$$

where ϵ is a UV cutoff in the dual BCFT_2. As described in [45,94], the length of the defect extremal surface $\mathcal{L}_1$ ending on the brane $\mathbb{Q}$ is given by

$$\mathcal{L}_1 = \ell \log\left(\frac{2b_1}{\epsilon}\right) + \ell \tanh^{-1}(\sin\theta_0). \quad (4.12)$$

Furthermore, the length of the defect extremal surface $\mathcal{L}_2$ may be obtained as follows [10]:

$$\mathcal{L}_2 = \ell \cosh^{-1}\left[\frac{(b_2 + b_1 \sin\theta_0)^2 + (b_1 \cos\theta_0)^2}{2\epsilon(b_1 \cos\theta_0)}\right]. \quad (4.13)$$

Note that, in this phase the interval A is very small and therefore we may approximate the above length in the following way:

$$\mathcal{L}_2 = \ell \cosh^{-1}\left(\frac{b_2^2 + b_1^2 + 2b_1 b_2 \sin\theta_0}{b_2^2 - b_1^2}\right) + \ell \log\left(\frac{b_2^2 - b_1^2}{\epsilon b_1}\right). \quad (4.14)$$

Now utilizing the identity $\cosh^{-1} x + \cosh^{-1} y = \cosh^{-1}(xy + \sqrt{(x^2-1)(y^2-1)})$ we finally obtain

$$\begin{aligned}\mathcal{L}_2 &= \ell\left[\cosh^{-1}\left(\frac{b_2^2 + b_1^2}{b_2^2 - b_1^2}\right) + \log\left(\frac{b_2^2 - b_1^2}{\epsilon b_1}\right) + \cosh^{-1}\left(\frac{1}{\cos\theta_0}\right)\right] \\ &= \ell \log\left(\frac{(b_1 + b_2)^2}{\epsilon b_1}\right) + \ell \tanh^{-1}(\sin\theta_0). \quad (4.15)\end{aligned}$$

Substituting Eqs. (4.11) and (4.15) in Eq. (4.10) we may now obtain the entanglement negativity between A and B in the bulk description as follows:

$$\mathcal{E}^{\mathrm{bulk}}(\mathcal{A}:\mathcal{B}) = \frac{3\ell}{4G_N} \log\left[\frac{(b_1 + b_2)(b_3 - b_1)}{2b_1(b_3 - b_2)}\right]. \quad (4.16)$$

Upon employing the Brown-Henneaux formula [170], we observe an exact matching with the island result in Eq. (4.9). Note that the above result is consistent with the geometric interpretation of the Markov gap as has explicitly been shown in Appendix A 1 through computation of the entanglement negativity by utilizing the alternative proposal in Eq. (2.14).

3. Phase-III

Boundary description. In the final phase both the intervals A and B are large enough to posses entanglement islands $I_A \equiv [-a, -a']$ and $I_B \equiv [-a', -\infty]$, respectively. They are also considered to be in proximity such that they have a connected entanglement wedge as shown in Fig. 6. The area term in Eq. (3.2) for the island cross section $\Gamma \equiv \partial I_A \cap \partial I_B$ is then given as [45,63,94]

$$\mathcal{A}(\Gamma) = \frac{\ell}{4G_N} \tanh^{-1}(\sin\theta_0). \quad (4.17)$$

The semiclassical effective entanglement negativity may be obtained in terms of the following five-point twist correlator

$$\begin{aligned}&\mathcal{E}^{\mathrm{eff}}(A \cup I_A : B \cup I_B) \\ &\quad = \lim_{n_e \to 1} \log[(\epsilon_y \Omega(-a))^{\Delta_{n_e}} (\epsilon_y \Omega(-a'))^{\Delta_{n_e}^{(2)}} \\ &\qquad \times \langle \mathcal{T}_{n_e}(b_1) \bar{\mathcal{T}}_{n_e}(-a) \bar{\mathcal{T}}_{n_e}(b_2) \mathcal{T}_{n_e}^2(-a') \bar{\mathcal{T}}_{n_e}(b_3) \rangle_{\mathrm{CFT}^{\otimes n_e}}],\end{aligned} \quad (4.18)$$

where ϵ_y is a UV regulator on the AdS_2 brane $\mathbb{Q}$ and the warp factor $\Omega(-a')$ is given in Eq. (4.2). The five-point twist correlator in Eq. (4.18) has the following factorization [164] in the corresponding OPE channel

$$\begin{aligned}&\langle \mathcal{T}_{n_e}(b_1) \bar{\mathcal{T}}_{n_e}(-a) \bar{\mathcal{T}}_{n_e}(b_2) \mathcal{T}_{n_e}^2(-a') \bar{\mathcal{T}}_{n_e}(b_3) \rangle \\ &\quad \approx \langle \mathcal{T}_{n_e}(b_1) \bar{\mathcal{T}}_{n_e}(-a) \rangle \langle \bar{\mathcal{T}}_{n_e}(b_2) \mathcal{T}_{n_e}^2(-a') \bar{\mathcal{T}}_{n_e}(b_3) \rangle \\ &\quad = \frac{1}{(a + b_1)^{2\Delta_{n_e}}} \frac{C_{\bar{\mathcal{T}}_{n_e} \mathcal{T}_{n_e}^2 \bar{\mathcal{T}}_{n_e}}}{(b_3 + a')^{\Delta_{n_e}^{(2)}} (b_2 + a')^{\Delta_{n_e}^{(2)}} (b_3 - b_2)^{2\Delta_{n_e} - \Delta_{n_e}^{(2)}}},\end{aligned} \quad (4.19)$$

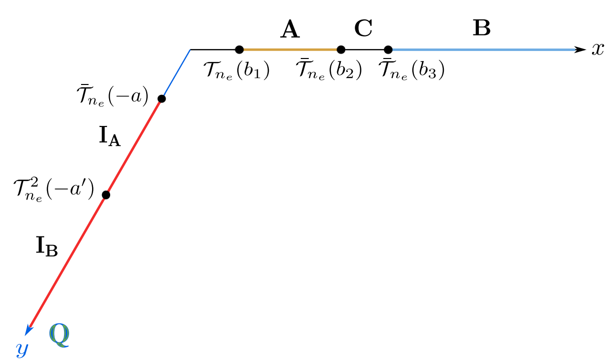

FIG. 6. Schematics of the quantum extremal surface for the entanglement negativity between two disjoint intervals A and B in phase-III. In this phase, we have a nontrivial island cross section on the brane at coordinate a'.

where Δ_{n_e} and $\Delta^{(2)}_{n_e}$ are the conformal dimensions of the twist operators $\mathcal{T}_{n_e}$ and $\mathcal{T}^2_{n_e}$, respectively, and are given as [137,138]

$$\Delta_{n_e} = \frac{c}{12}\left(1 - \frac{1}{n_e}\right), \qquad \Delta^{(2)}_{n_e} = \frac{c}{6}\left(\frac{n_e}{2} - \frac{2}{n_e}\right). \tag{4.20}$$

Note that the point a on the brane is determined by the DES for the subsystem A to be $a = b_1$ [45]. Therefore, by utilizing the contractions in (4.19) along with the areas term in Eq. (4.17), we may obtain the generalized negativity in the boundary description from Eq. (3.1) to be

$$\mathcal{E}^{\rm bdy}_{\rm gen}(A:B) = \frac{c}{4}\left[\tanh^{-1}(\sin\theta_0) + \log\frac{\ell(b_2 + a')(b_3 + a')}{a'(b_3 - b_2)\epsilon_y \cos\theta_0}\right]. \tag{4.21}$$

The extremization with respect to the island cross section Γ with the coordinate a' on the brane leads to

$$\partial_{a'}\mathcal{E}^{\rm bdy}_{\rm gen} = 0 \Rightarrow a' = \sqrt{b_2 b_3}. \tag{4.22}$$

Substituting this into Eq. (4.21), we may obtain the total entanglement negativity between A and B in phase-III from the boundary description to be

$$\mathcal{E}^{\rm bdy}(A:B) = \frac{c}{4}\left[\tanh^{-1}(\sin\theta_0) + \log\left(\frac{\sqrt{b_3} + \sqrt{b_2}}{\sqrt{b_3} - \sqrt{b_2}}\right) + \log\left(\frac{\ell}{\epsilon_y \cos\theta_0}\right)\right]. \tag{4.23}$$

Bulk description. The bulk description in phase-III consists of a connected entanglement wedge and the minimal cross section ends on the EOW brane. The configuration is sketched in Fig. 7. Since the bulk quantum matter is entirely situated on the EOW brane, the effective entanglement negativity between the bulk quantum matter fields in the bulk regions $\mathcal{A}$ and $\mathcal{B}$ reduces to the effective matter negativity between the corresponding island regions I_A and I_B,

$$\begin{aligned}\mathcal{E}^{\rm eff}(\mathcal{A}:\mathcal{B}) &\equiv \mathcal{E}^{\rm eff}(I_A:I_B) \\ &= \lim_{n_e\to 1} \log\left[(\epsilon_y\Omega(-a'))^{\Delta^{(2)}_{n_e}} \langle \mathcal{T}_{n_e}(-b_1)\bar{\mathcal{T}}^2_{n_e}(-a')\rangle_{{\rm BCFT}^{\otimes n_e}}\right],\end{aligned} \tag{4.24}$$

where ϵ_y is the UV cutoff on the EOW brane and Ω is the conformal factor as given in Eq. (4.2). Utilizing the doubling trick [123,127] the above two-point function in the defect BCFT_2 may be reduced to a four-point correlator of chiral twist fields in a CFT_2 defined on the whole complex plane. As described in [127], the four-point correlator in the chiral CFT_2 has two dominant channels depending on the cross-ratio as follows:

(I) *BOE channel*: In this channel the two point correlator factorizes into two one-point functions in the BCFT_2 as follows:

$$\begin{aligned}&\langle \mathcal{T}_{n_e}(b_1)\bar{\mathcal{T}}^2_{n_e}(-a')\rangle_{{\rm BCFT}^{\otimes n_e}} \\ &\quad= \langle \mathcal{T}_{n_e}(-b_1)\rangle_{{\rm BCFT}^{\otimes n_e}} \langle \bar{\mathcal{T}}^2_{n_e}(-a')\rangle_{{\rm BCFT}^{\otimes n_e}} \\ &\quad= \frac{\epsilon_y^{\Delta_{n_e}+\Delta^{(2)}_{n_e}}}{(2b_1)^{\Delta_{n_e}}(2a')^{\Delta^{(2)}_{n_e}}}.\end{aligned} \tag{4.25}$$

Therefore, the effective bulk entanglement negativity in this phase is given by

$$\mathcal{E}^{\rm eff}(I_A:I_B) = \frac{c}{4}\log\frac{2\ell}{\epsilon_y\cos\theta_0}. \tag{4.26}$$

Note that this effective entanglement negativity is equal to the Rényi entropy of order one half for the interval I_A (or I_B) which is consistent with the expectations from quantum information theory.

(II) *OPE channel*: In this channel, the two-point correlator of twist fields on the BCFT_2 reduces to a three-point correlator of chiral twist fields on the full complex plane as follows [63,123,127]:

$$\begin{aligned}&\langle \mathcal{T}_{n_e}(-b_1)\bar{\mathcal{T}}^2_{n_e}(-a')\rangle_{{\rm BCFT}^{\otimes n_e}} \\ &\quad= \langle \bar{\mathcal{T}}_{n_e}(-b_1)\mathcal{T}_{n_e}(b_1)\bar{\mathcal{T}}^2_{n_e}(-a')\rangle_{{\rm CFT}^{\otimes n_e}} \\ &\quad= \frac{C_{\bar{\mathcal{T}}_{n_e}\mathcal{T}^2_{n_e}\bar{\mathcal{T}}_{n_e}}}{(a'^2 - b_1^2)^{\Delta^{(2)}_{n_e}}(2b_1)^{\Delta^{(2)}_{n_e}-2\Delta_{n_e}}}.\end{aligned} \tag{4.27}$$

Therefore, the effective bulk entanglement negativity in this channel is given by

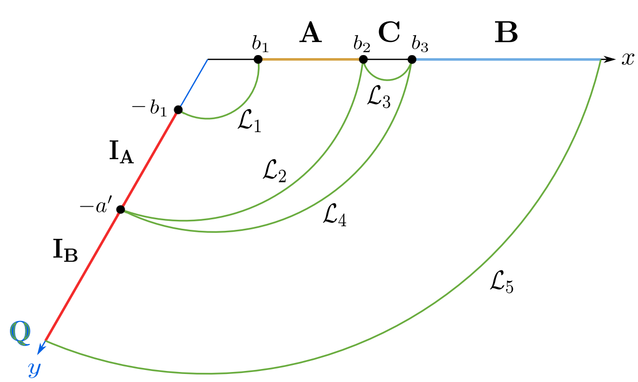

FIG. 7. Schematics of the defect extremal surface for the entanglement negativity between two disjoint intervals A and B in phase-III. In this phase, the EWCS ends on the island cross section Γ on the EOW brane.

$$\mathcal{E}^{\mathrm{eff}}(I_A:\, I_B) = \frac{c}{4}\log\left[\frac{\ell(a'^2 - b_1^2)}{a' b_1 \epsilon_y \cos\theta_0}\right]. \tag{4.28}$$

As shown in Fig. 7, the contribution to the bulk entanglement negativity from the defect extremal surfaces homologous to different combinations of subsystems is given by

$$\begin{aligned}\frac{3}{16G_N}(\mathcal{L}_2 + \mathcal{L}_4 - \mathcal{L}_3) &= \frac{3\ell}{16G_N}\left[\cosh^{-1}\left\{\frac{(b_2 + a'\sin\theta_0)^2 + (a'\cos\theta_0)^2}{2\epsilon(a'\cos\theta_0)}\right\}\right. \\ &\quad + \cosh^{-1}\left\{\frac{(b_3 + a'\sin\theta_0)^2 + (a'\cos\theta_0)^2}{2\epsilon(a'\cos\theta_0)}\right\} \\ &\quad \left. - 2\log\left(\frac{b_3 - b_2}{\epsilon}\right)\right].\end{aligned} \tag{4.29}$$

The entanglement negativity between the disjoint intervals A and B is obtained by extremizing the generalized negativity over the position of the island cross section Γ. For the OPE channel of the effective bulk entanglement negativity there is no extremal solution while for the BOE channel we obtain

$$\partial_{a'}\mathcal{E}^{\mathrm{bulk}}_{\mathrm{gen}} = 0 \Rightarrow a' = \sqrt{b_2 b_3}. \tag{4.30}$$

Substituting this and utilizing the proximity limit $b_3 \to b_2$ in the intermediate step, we obtain the entanglement negativity between A and B in the bulk description as follows:

$$\begin{aligned}\mathcal{E}^{\mathrm{bulk}} &= \frac{3\ell}{16G_N}\left[\cosh^{-1}\left(\frac{b_2 + b_3 + 2\sqrt{b_2 b_3}\sin\theta_0}{(b_3 - b_2)\cos\theta_0}\right)\right] \\ &\quad + \frac{c}{4}\log\left(\frac{\ell}{\epsilon_y\cos\theta_0}\right) \\ &= \frac{3\ell}{16G_N}\left[\log\left(\frac{\sqrt{b_3} + \sqrt{b_2}}{\sqrt{b_3} - \sqrt{b_2}}\right) + \cosh^{-1}\left(\frac{1}{\cos\theta_0}\right)\right] \\ &\quad + \frac{c}{4}\log\left(\frac{\ell}{\epsilon_y\cos\theta_0}\right).\end{aligned} \tag{4.31}$$

The above expression for the holographic entanglement negativity matches exactly with the QES result in Eq. (4.23) obtained through the island formula Eq. (3.1). This provides yet another consistency check of our holographic construction for the entanglement negativity in the defect $\mathrm{AdS}_3/\mathrm{BCFT}_2$ scenario. We should also note that Eq. (4.31) is consistent with the geometric computation of the Markov gap as demonstrated in Appendix A 1.

B. Two adjacent intervals

Having computed the entanglement negativity for configurations involving two disjoint intervals, we now turn our attention to the mixed state of two adjacent intervals $A = [0, b_1]$ and $B = [b_1, b_2]$ on a fixed time slice in the $\mathrm{AdS}_3/\mathrm{BCFT}_2$ model. The interval A in this case always possess an entanglement island as it starts from the interface between the EOW brane and the asymptotic boundary. We however, have two possible phases for this case based on the size of the interval B which are described below.

1. Phase-I

Boundary description. For this phase, we consider that the interval B is large enough to posses an entanglement island described as I_B in Fig. 8. The area term in Eq. (3.2) for the point $\Gamma = \partial I_A \cap \partial I_B$ is as given in Eq. (2.8). The effective semiclassical entanglement negativity is given by the following two-point twist correlator

$$\begin{aligned}&\mathcal{E}^{\mathrm{eff}}(A \cup I_A:\, B \cup I_B) \\ &\quad = \lim_{n_e \to 1}\log\left[(\epsilon_y\Omega(-a))^{\Delta^{(2)}_{n_e}}\langle \mathcal{T}^2_{n_e}(b_1)\bar{\mathcal{T}}^2_{n_e}(-a)\rangle_{\mathrm{CFT}^{\otimes n_e}}\right] \\ &\quad = \frac{c}{4}\log\left[\frac{\ell(b_1 + a)^2}{\epsilon\,\epsilon_y a\cos\theta_0}\right],\end{aligned} \tag{4.32}$$

where ϵ and ϵ_y are the UV cutoffs on the asymptotic boundary and the EOW brane $\mathbb{Q}$, respectively, and the warp factor $\Omega(a)$ is as given in Eq. (4.2). The point $a = b_1$ on the brane is determined through the entanglement entropy computation of the interval A. Using this in Eq. (4.32) along with the area term, we may obtain the total entanglement negativity in the boundary description to be

$$\begin{aligned}\mathcal{E}^{\mathrm{bdy}}(A{:}B) = \frac{c}{4}\left[\log\left(\frac{2b_1}{\epsilon}\right) + \log\left(\frac{2\ell}{\epsilon_y\cos\theta_0}\right)\right. \\ \left. + \tanh^{-1}(\sin\theta_0)\right],\end{aligned} \tag{4.33}$$

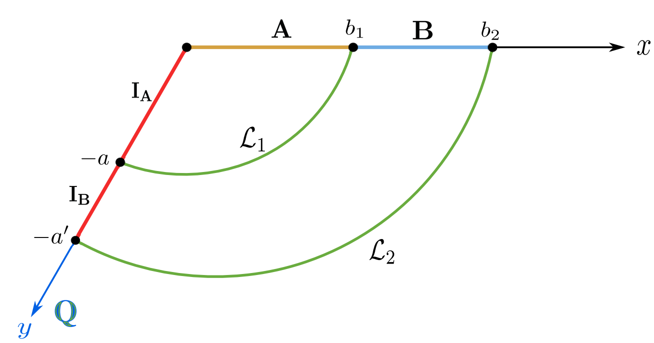

FIG. 8. Schematics of the defect extremal surface for the entanglement negativity between two adjacent intervals A and B in phase-I. I_A and I_B on the EOW brane describe the entanglement island corresponding to intervals A and B, respectively.

where we have used the Brown-Henneaux formula in the area term [170].

Bulk description. In the double holographic description, the entanglement wedge corresponding to the subsystem $A \cup B$ is connected in the bulk. The contribution to the effective entanglement negativity between the bulk matter fields in regions $\mathcal{A}$ and $\mathcal{B}$ arises solely from the quantum matter fields situated on the EOW brane as follows:

$$\begin{aligned}\mathcal{E}^{\mathrm{eff}}(\mathcal{A}:\mathcal{B}) &= \mathcal{E}^{\mathrm{eff}}(I_A:\, I_B) \\ &= \lim_{n_e\to 1}\log\left[(\epsilon_y\Omega(-a))^{\Delta^{(2)}_{n_e}}\langle\mathcal{T}_{n_e}(-a')\bar{\mathcal{T}}^2_{n_e}(-a)\rangle_{\mathrm{BCFT}^{\otimes n_e}}\right] \\ &= \frac{c}{4}\log\left(\frac{2\ell}{\epsilon_y\cos\theta_0}\right).\end{aligned} \tag{4.34}$$

Utilizing Eq. (3.4), the total entanglement negativity for this case including the contribution from the combinations of the bulk extremal curves is obtained to be

$$\begin{aligned}\mathcal{E}^{\mathrm{bulk}}(A:B) &= \mathcal{E}^{\mathrm{eff}}(\mathcal{A}:\mathcal{B}) + \frac{3}{16G_N}2\mathcal{L}_1 \\ &= \frac{c}{4}\log\left(\frac{2\ell}{\epsilon_y\cos\theta_0}\right) \\ &\quad + \frac{3\ell}{8G_N}\left[\log\left(\frac{2b_1}{\epsilon}\right) + \tanh^{-1}(\sin\theta_0)\right],\end{aligned} \tag{4.35}$$

where we have used the fact that the entanglement entropy computation for the interval A fixes $a = b_1$. On utilization of the Brown-Henneaux formula [170], the above expression matches exactly with the result obtained from the boundary perspective in Eq. (4.33). Also note that for the configuration under consideration, the Markov recovery process is perfect as there are no nontrivial boundaries of the corresponding EWCS which has also been shown in Appendix A 2.

2. Phase-II

Boundary description. For this phase, we now consider the case where the interval B is small such that it lacks an entanglement entropy island as shown in Fig. 9. This implies that the island cross section Γ is a null set. The remaining effective semiclassical entanglement negativity is obtained through the following three-point twist correlator

$$\begin{aligned}&\mathcal{E}^{\mathrm{eff}}(A\cup I_A : B\cup I_B) \\ &= \lim_{n_e\to 1}\log\left[(\epsilon_y\Omega(-a))^{\Delta_{n_e}}\langle\mathcal{T}_{n_e}(-a)\bar{\mathcal{T}}^2_{n_e}(b_1)\mathcal{T}_{n_e}(b_2)\rangle_{\mathrm{CFT}^{\otimes n_e}}\right] \\ &= \frac{c}{4}\log\left[\frac{(b_1+a)(b_2-b_1)}{(b_2+a)\epsilon}\right].\end{aligned} \tag{4.36}$$

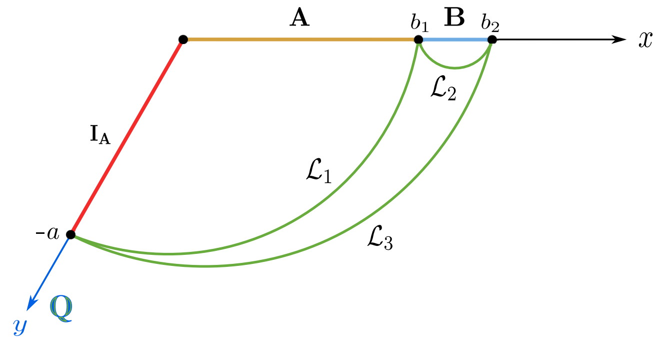

FIG. 9. Schematics of the defect extremal surface for the entanglement negativity between two adjacent intervals A and B in phase-II. In this phase, the island of the interval B is an empty set.

Again, the point on the AdS_2 brane $\mathbb{Q}$ is fixed to be $a = b_1$ through the entanglement entropy computation of the interval A. Utilizing this value of a, we may obtain the total entanglement negativity for this phase in the boundary description to be

$$\mathcal{E}^{\mathrm{bdy}}(A:B) = \frac{c}{4}\log\left[\frac{2b_1(b_2-b_1)}{(b_2+b_1)\epsilon}\right]. \tag{4.37}$$

Bulk description. For the bulk description of this phase, we observe in Fig. 9 that the entanglement wedge for the subsystem $A \cup B$ is connected. However, since the interval B does not have an entanglement island, the effective entanglement negativity term in Eq. (3.4) vanishes. The only contribution to the total entanglement negativity comes from the lengths of the extremal curves labeled as $\mathcal{L}_i$ ($i = 1, 2, 3$) in Fig. 9. To this end, we note that the lengths of the extremal curves $\mathcal{L}_1$ and $\mathcal{L}_2$ have the same form as given in Eqs. (4.12) and (4.11), respectively. Using similar approximations as were employed for the bulk description in Sec. IV A 2, the length of the extremal curve $\mathcal{L}_3$ may be computed to be

$$\mathcal{L}_3 = \ell\,\log\left(\frac{(b_1+b_2)^2}{\epsilon b_1}\right) + \ell\tanh^{-1}(\sin\theta_0), \tag{4.38}$$

where we have used $a = b_1$. We may now obtain the total entanglement negativity for this phase using Eq. (3.4) to be

$$\mathcal{E}^{\mathrm{bdy}}(A:B) = \frac{3\ell}{8G_N}\log\left[\frac{2b_1(b_2-b_1)}{(b_2+b_1)\epsilon}\right], \tag{4.39}$$

which on utilization of the usual Brown-Henneaux formula [170] matches exactly with the result obtained through the boundary description in Eq. (4.37). We also note here that the above result differs from the corresponding reflected

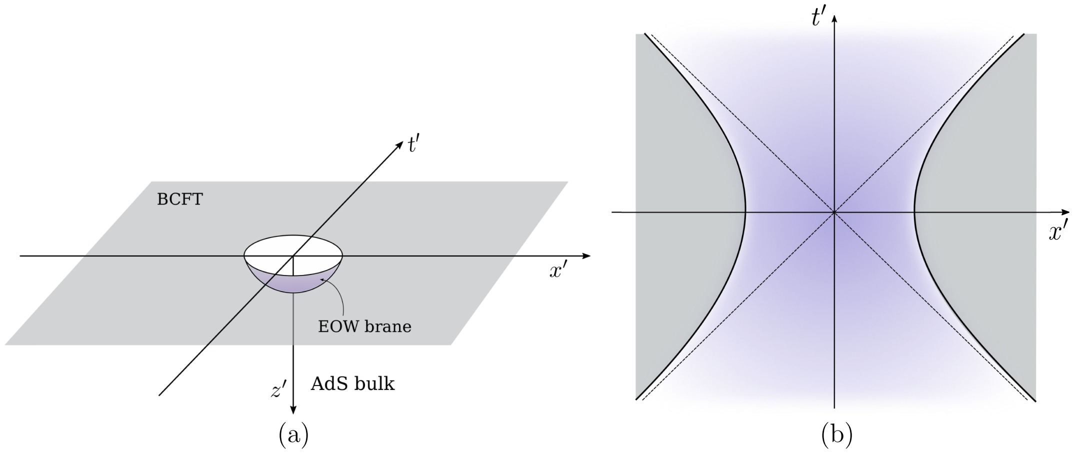

FIG. 10. (a) Euclidean AdS/BCFT with the BCFT defined outside the circle. (b) 2d eternal black hole in Lorentzian signature.

entropy by an additive constant described by the Markov gap. This has also been discussed in Appendix A 2.

V. TIME-DEPENDENT ENTANGLEMENT NEGATIVITY IN BLACK HOLES

In this section we investigate the nature of mixed-state entanglement through the entanglement negativity in a time-dependent defect $\mathrm{AdS}_3/\mathrm{BCFT}_2$ scenario involving an eternal black hole in the effective two-dimensional description [63,94]. The lower-dimensional effective model involves the appearance of entanglement islands during the emission of the Hawking radiation from the eternal black hole.

A. Review of the eternal black hole in AdS/BCFT

As described in [63,94], we consider a BCFT_2 defined on the half-plane $(x, \tau \geq 0)$. The corresponding bulk dual is described by the Poincaré-AdS_3 geometry truncated by an end-of-the-world brane located at the hypersurface $\tau = -z\tan\theta_0$. Here θ_0 is the angle made by the EOW brane with the vertical, and τ and z are the timelike[14] and holographic coordinates, respectively.

Utilizing a global conformal map, the boundary of the BCFT_2 is then mapped to a circle

$$x'^2 + \tau'^2 = 1. \tag{5.1}$$

The bulk dual of such a global conformal transformation is given by the following Banados map [63,94,124]

$$\tau' = 1 + \frac{\tau - \frac{1}{2}(\tau^2 + x^2 + z^2)}{1 - \tau + \frac{1}{4}(\tau^2 + x^2 + z^2)},$$
$$x' = \frac{x}{1 - \tau + \frac{1}{4}(\tau^2 + x^2 + z^2)},$$
$$z' = \frac{z}{1 - \tau + \frac{1}{4}(\tau^2 + x^2 + z^2)}. \tag{5.2}$$

The EOW brane is mapped to a portion of a sphere under these bulk transformations,

$$x'^2 + \tau'^2 + (z' + \tan\theta_0)^2 = \sec^2\theta_0. \tag{5.3}$$

Note that, as the above transformation is a global conformal map, the metric in the bulk dual spacetime as well as the metric induced on the EOW brane are preserved under the Banados map Eq. (5.2). The schematics of this time-dependent AdS/BCFT scenario is depicted in Fig. 10(a).

Finally employing the partial Randall-Sundrum reduction combined with the $\mathrm{AdS}_3/\mathrm{BCFT}_2$ correspondence discussed in [45,63,94], one obtains a two-sided $(1+1)$-dimensional eternal black hole on the EOW brane which is coupled to the BCFT_2 outside the circle [Eq. (5.1)] in the $2d$ effective description. The schematics of the configuration is depicted in Fig. 10(b). The hybrid manifold consisting of a $2d$ eternal black hole with a fluctuating geometry coupled to the flat BCFT_2 may conveniently be described in terms of the Rindler coordinates (X, T) defined through

$$x' = e^X \cosh T, \qquad t' \equiv -i\tau' = e^X \sinh T. \tag{5.4}$$

These Rindler coordinates naturally capture the near-horizon geometry of the $2d$ black hole [94].

In the following, we will compute the entanglement negativity for various bipartite states involving two disjoint and two adjacent intervals in the time-dependent scenario of defect AdS/BCFT discussed above. In this regard, we

[14]Note that in the Euclidean signature, there is no essential difference between the timelike and spacelike coordinates and the present parametrization is a convenient choice adapted in [63,94].

will employ the semiclassical island formula Eq. (3.2) in the lower-dimensional effective description as well as the doubly holographic defect extremal surface proposals in Eqs. (3.3) and (3.4) and find exact agreement between the two.

B. Entanglement negativity between black hole interiors

In this subsection, we compute the time-dependent entanglement negativity between different regions of the black hole interior. As described in [63,94] the black hole region B is defined as the spacelike interval from $Q \equiv (t'_0, -x'_0)$ to $P \equiv (t'_0, x'_0)$ as shown in Fig. 11. We perform the computations in the Euclidean signature with $\tau'_0 = it'_0$ and subsequently obtain the final result in Lorentzian signature through an analytic continuation. Depending on the configuration of the extremal surface for the entanglement entropy of B, there are two possible phases for the extremal surfaces corresponding to the entanglement negativity between the black hole subsystems B_L and B_R.

1. Connected phase

The connected phase corresponds to the scenario where there is no entanglement island for the radiation bath in the effective boundary description as shown in Fig. 11. From the bulk perspective, this corresponds to a connected extremal surface for $B_L \cup B_R$. In this phase, it is required to compute the entanglement negativity between the two adjacent intervals $B_L \equiv |O'Q|$ and $B_R \equiv |O'P|$, where the point O' is dynamical as it resides on the EOW brane with a gravitational theory.

Boundary description. In the $2d$ boundary description, the effective semiclassical entanglement negativity between B_L and B_R may be computed through the three-point correlation function of twist operators as follows:

$$\mathcal{E}^{\mathrm{eff}}(B_L : B_R) = \lim_{n_e \to 1} \log[(\epsilon_y \Omega_{O'})^{\Delta^{(2)}_{n_e}} \langle \mathcal{T}_{n_e}(Q) \bar{\mathcal{T}}^2_{n_e}(O') \mathcal{T}_{n_e}(P) \rangle]. \tag{5.5}$$

It is convenient to perform the computations in the unprimed coordinates (y, x) given in Eq. (2.2), where y measures the distance along the EOW brane and x is the spatial coordinate

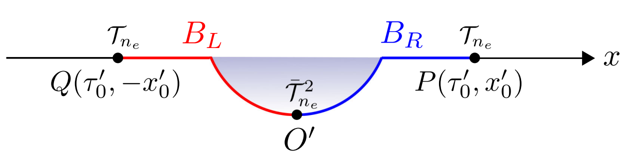

FIG. 11. Schematics of the quantum extremal surface for the entanglement negativity between black hole interiors in the connected phase at a constant time slice.

describing the BCFT$_2$. In these coordinates, the conformal factor associated with the dynamical point O' on the EOW brane $\mathbb{Q}$ is given by [45,63,94]

$$\Omega_{O'}(y) = \left| \frac{y \cos\theta_0}{\ell} \right|. \tag{5.6}$$

where ℓ is the AdS$_3$ radius inherited from the bulk geometry. The form of the CFT$_2$ three-point function in Eq. (5.5) is given by

$$\langle \mathcal{T}_{n_e}(Q) \bar{\mathcal{T}}^2_{n_e}(O') \mathcal{T}_{n_e}(P) \rangle = C_{\mathcal{T}_{n_e}\mathcal{T}^2_{n_e}\mathcal{T}_{n_e}} |O'P|^{-\Delta^{(2)}_{n_e}} |O'Q|^{-\Delta^{(2)}_{n_e}} |PQ|^{-2\Delta_{n_e} + \Delta^{(2)}_{n_e}}, \tag{5.7}$$

where $C_{\mathcal{T}_{n_e}\mathcal{T}^2_{n_e}\mathcal{T}_{n_e}}$ is the constant OPE coefficient which is neglected henceforth. Substituting Eqs. (5.6) and (5.7) in Eq. (5.5), we may obtain the following expression for the generalized entanglement negativity between B_L and B_R in the boundary description

$$\mathcal{E}^{\mathrm{bdy}}_{\mathrm{gen}}(B_L : B_R) = \frac{c}{4} \log\left[\frac{(\tau_0 + y)^2 + x_0^2}{2x_0}\right] + \frac{c}{4} \log\left(\frac{\ell}{\epsilon_y y \cos\theta_0}\right) + \frac{c}{4} \tanh^{-1}(\sin\theta_0), \tag{5.8}$$

where we have added the area term Eq. (2.8) corresponding to the point O' on the EOW brane in the QES formula. The above expression is extremized over the position y of the dynamical point O' to obtain

$$y_0 = \sqrt{\tau_0^2 + x_0^2}. \tag{5.9}$$

Substituting the above expression in Eq. (5.8), the semiclassical entanglement negativity in the $2d$ effective boundary description is obtained as follows:

$$\mathcal{E}^{\mathrm{bdy}}(B_L : B_R) = \frac{c}{4} \log\left[\frac{\tau_0 + \sqrt{\tau_0^2 + x_0^2}}{x_0}\right] + \frac{c}{4} \log\left(\frac{\ell}{\epsilon_y \cos\theta_0}\right) + \frac{c}{4} \tanh^{-1}(\sin\theta_0). \tag{5.10}$$

Now transforming back to the primed coordinates using Eq. (5.2) and analytically continuing to the Lorentzian signature, the above expression reduces to

$$\mathcal{E}^{\mathrm{bdy}}(B_L : B_R) = \frac{c}{4} \log\left[\frac{x_0'^2 - t_0'^2 - 1 + \sqrt{4x_0'^2 + (x_0'^2 - t_0'^2 - 1)^2}}{2x'_0}\right] + \frac{c}{4} \log\left(\frac{\ell}{\epsilon_y \cos\theta_0}\right) + \frac{c}{4} \tanh^{-1}(\sin\theta_0). \tag{5.11}$$

In terms of the Rindler coordinates (X, T), the final result for the entanglement negativity between the black hole interiors becomes

$$\mathcal{E}^{\mathrm{bdy}}(B_L:B_R) = \frac{c}{4}\log\left[\frac{e^{2X_0}-1+\sqrt{4e^{2X_0}\cosh^2 T+(e^{2X_0}-1)^2}}{2e^{X_0}\cosh T}\right] + \frac{c}{4}\log\left(\frac{\ell}{\epsilon_y\cos\theta_0}\right) + \frac{c}{4}\log\left(\frac{\cos\theta_0}{1-\sin\theta_0}\right), \tag{5.12}$$

where X_0 describes the boundary of the black hole region at a fixed Rindler time T. Note that the above expression for the entanglement negativity between B_L and B_R is a decreasing function of the Rindler time T in this phase.

Bulk description. Next we focus on the three-dimensional bulk description for the connected phase of the entanglement negativity between the black hole interiors. To compute the holographic entanglement negativity, we note that the mixed-state configuration described by B_L and B_R corresponds to the case of two adjacent intervals $|O'P|$ and $|O'Q|$. The configuration of the bulk extremal curves homologous to various subsystems under consideration is depicted in Fig. 12. Now employing the DES formula given in Eq. (3.4), we may obtain

$$\mathcal{E}^{\mathrm{bulk}}_{\mathrm{gen}}(\mathcal{B}_L:\mathcal{B}_R) = \frac{3}{16G_N}(\mathcal{L}_1+\mathcal{L}_2-\mathcal{L}_3) + \mathcal{E}^{\mathrm{eff}}(\mathcal{B}_L:\mathcal{B}_R), \tag{5.13}$$

where $\mathcal{L}_1$, $\mathcal{L}_2$ and $\mathcal{L}_3$ are the lengths of the bulk extremal curves homologous to $|O'P|$, $|O'Q|$ and $|PQ|$, respectively, and $\mathcal{E}^{\mathrm{eff}}(\mathcal{B}_L:\mathcal{B}_R)$ denotes the effective entanglement negativity between bulk quantum matter fields residing on the EOW brane.

In the unprimed coordinates, the Cauchy slice on the EOW brane is in a pure state as described in [63]. Hence, the effective entanglement negativity in Eq. (5.13) may be obtained through the Rényi entropy of order one half for a part of matter fields on the EOW brane. Consequently, similar to Eq. (4.26), the effective entanglement negativity is a constant given by

$$\mathcal{E}^{\mathrm{eff}}(\mathcal{B}_L:\mathcal{B}_R) = \frac{c}{4}\log\frac{2\ell}{\epsilon_y\cos\theta_0}. \tag{5.14}$$

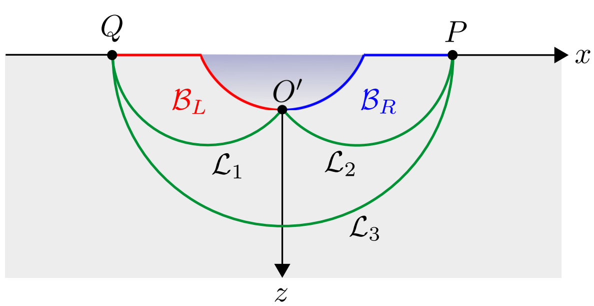

FIG. 12. Schematics of the defect extremal surface for the entanglement negativity between black hole interiors in the connected phase. The bulk extremal curves homologous to B_L, B_R and $B_L\cup B_R$ are given by $\mathcal{L}_1$, $\mathcal{L}_2$ and $\mathcal{L}_3$ respectively.

As the effective entanglement negativity turns out to be a constant, the entanglement negativity in this phase is determined entirely through the algebraic sum of the lengths of the extremal curves in Eq. (5.13). To obtain the lengths of these extremal curve, we employ the unprimed coordinate system with the Poincaré-AdS$_3$ metric [63]. Under the bulk map in Eq. (5.2), the coordinates of P and Q may be mapped to $(\tau_0, x_0, 0)$ and $(\tau_0, -x_0, 0)$ where

$$\tau_0 = \frac{2(x_0'^2+\tau_0'^2-1)}{(\tau_0'+1)^2+x_0'^2}, \qquad x_0 = \frac{4x_0'}{(\tau_0'+1)^2+x_0'^2}. \tag{5.15}$$

Utilizing the left-right $\mathbb{Z}_2$ symmetry of the configuration, we may set the coordinates of the dynamical point O' on the brane as O': $(-z\tan\theta_0, 0, z)$, where z is determined through the extremization of the generalized negativity functional in Eq. (5.13). The lengths of the extremal curves may now be obtained in the unprimed coordinates through the standard Poincaré-AdS$_3$ result as follows [10,11]:

$$\begin{aligned}\mathcal{L}_1 &= \ell\cosh^{-1}\left[\frac{(\tau_0+z\tan\theta_0)^2+x_0^2+z^2}{2z}\right] - \ell\log\left[\frac{4\epsilon}{(\tau_0'+1)^2+x_0'^2}\right] = \mathcal{L}_2,\\ \mathcal{L}_3 &= 2\ell\log(2x_0) - 2\ell\log\left[\frac{4\epsilon}{(\tau_0'+1)^2+x_0'^2}\right].\end{aligned} \tag{5.16}$$

In the above expression, ϵ is the UV cutoff for the original BCFT$_2$ in the primed coordinates and the second logarithmic term arises due to the cutoff in the unprimed coordinates [cf. the Banados map in Eq. (5.2)]. Now extremizing the generalized negativity with respect to z we may obtain the position of O' to be

$$\partial_z\mathcal{E}^{\mathrm{bulk}}_{\mathrm{gen}} = 0 \Rightarrow z = \sqrt{x_0^2+\tau_0^2}\cos\theta_0. \tag{5.17}$$

Substituting the above value of z in Eq. (5.13), we may obtain the bulk entanglement negativity between $\mathcal{B}_L$ and $\mathcal{B}_R$ as follows:

$$\mathcal{E}^{\mathrm{bulk}}(\mathcal{B}_L:\mathcal{B}_R) = \frac{c}{4}\left[\cosh^{-1}\left(\frac{\sqrt{x_0^2+\tau_0^2}+\tau_0\sin\theta_0}{x_0\cos\theta_0}\right) + \log\frac{\ell}{\epsilon_y\cos\theta_0}\right], \tag{5.18}$$

where the effective contribution from the quantum matter fields given in Eq. (5.14) has been included. Now utilizing the hyperbolic identity

$$\cosh^{-1}\left(\frac{\sqrt{x_0^2+\tau_0^2}+\tau_0\sin\theta_0}{x_0\cos\theta_0}\right) = \log\left(\frac{\tau_0+\sqrt{x_0^2+\tau_0^2}}{x_0}\right)+\cosh^{-1}(\sec\theta_0), \tag{5.19}$$

Eq. (5.18) may be expressed as

$$\mathcal{E}^{\mathrm{bulk}}(\mathcal{B}_L:\mathcal{B}_R)=\frac{c}{4}\left[\log\left(\frac{\tau_0+\sqrt{x_0^2+\tau_0^2}}{x_0}\right)+\log\frac{\ell}{\epsilon_y\cos\theta_0} + \log\frac{\cos\theta_0}{1-\sin\theta_0}\right]. \tag{5.20}$$

Transforming to the primed coordinates using Eq. (5.2) and subsequently to the Rindler coordinates Eq. (5.4) via the analytic continuation $\tau' = it'$, we may obtain the bulk entanglement negativity between $\mathcal{B}_L$ and $\mathcal{B}_R$ to be

$$\mathcal{E}^{\mathrm{bulk}}(\mathcal{B}_L:\ \mathcal{B}_R) = \frac{c}{4}\log\left[\frac{e^{2X_0}-1+\sqrt{4e^{2X_0}\cosh^2T+(e^{2X_0}-1)^2}}{2e^{X_0}\cosh T}\right] + \frac{c}{4}\log\left(\frac{\ell}{\epsilon_y\cos\theta_0}\right)+\frac{c}{4}\log\left(\frac{\cos\theta_0}{1-\sin\theta_0}\right). \tag{5.21}$$

The above expression matches identically with the boundary QES result in Eq. (5.12) which provides a strong consistency check of our holographic construction. Also note that the above result for the entanglement negativity differs from the corresponding reflected entropy computed earlier in [63] by a constant factor of $\frac{c}{4}\log 2$ which is consistent with the geometric interpretation of the Markov gap as discussed in Sec. II D.

2. Disconnected phase

In this subsection, we concentrate on the disconnected phase for the extremal surface for $B_L \cup B_R$, depicted in Fig. 13. In this case, there are entanglement islands corresponding to the radiation bath on the EOW brane, and a part of the entanglement wedge for the radiation bath is subtended on the brane. This splits the black hole regions into two disjoint subsystems, namely $B_R \equiv |PP'|$ and $B_L \equiv |QQ'|$, where the points P' and Q' are determined by the extremal surface for $B_L \cup B_R$.

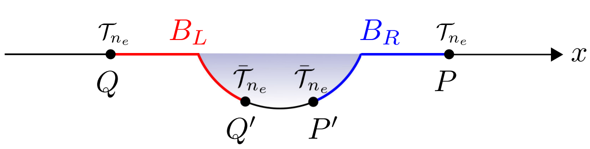

FIG. 13. Schematics of the quantum extremal surface for the entanglement negativity between black hole interiors in the disconnected phase.

Boundary description. In the two-dimensional effective boundary description, the area term for the generalized entanglement negativity vanishes since there is no nontrivial island cross section, $\partial B_L \cap \partial B_R = \varnothing$. The effective semiclassical entanglement negativity between B_L and B_R may be computed through the following four-point correlator of twist operators placed at the endpoints of the intervals,

$$\mathcal{E}^{\mathrm{eff}}(B_L:\ B_R) = \lim_{n_e\to 1}\log[(\epsilon_y\Omega_{P'})^{\Delta_{n_e}}(\epsilon_y\Omega_{Q'})^{\Delta_{n_e}} \times\langle\mathcal{T}_{n_e}(Q)\bar{\mathcal{T}}_{n_e}(Q')\bar{\mathcal{T}}_{n_e}(P')\mathcal{T}_{n_e}(P)\rangle]. \tag{5.22}$$

As indicated by the disconnected extremal surfaces shown in Fig. 13, the above four-point correlator factorizes into the product of two 2-point correlators as follows:

$$\langle\mathcal{T}_{n_e}(Q)\bar{\mathcal{T}}_{n_e}(Q')\bar{\mathcal{T}}_{n_e}(P')\mathcal{T}_{n_e}(P)\rangle \approx \langle\mathcal{T}_{n_e}(Q)\bar{\mathcal{T}}_{n_e}(Q')\rangle\langle\mathcal{T}_{n_e}(P)\bar{\mathcal{T}}_{n_e}(P')\rangle. \tag{5.23}$$

Now utilizing Eq. (4.20), we may observe that, in the replica limit $n_e \to 1$, the above correlation function vanishes identically. Hence, in this phase the total entanglement negativity between the black hole interiors is also vanishing.

Bulk description. As depicted in Fig. 14, the entanglement wedges corresponding to the subsystems B_L and B_R are naturally disconnected and hence, the configuration corresponds to two disjoint intervals on the boundary which are far away from each other. In this case, the area contribution to the bulk entanglement negativity vanishes [151,152]. The effective entanglement negativity between portions of bulk quantum matter on the EOW brane is given by the BCFT correlation function of twist fields inserted at P' and Q' as follows:

$$\mathcal{E}^{\mathrm{eff}} = \lim_{n_e\to 1}\log\langle\mathcal{T}_{n_e}(P')\bar{\mathcal{T}}_{n_e}(Q')\rangle_{\mathrm{BCFT}^{\otimes n_e}}. \tag{5.24}$$

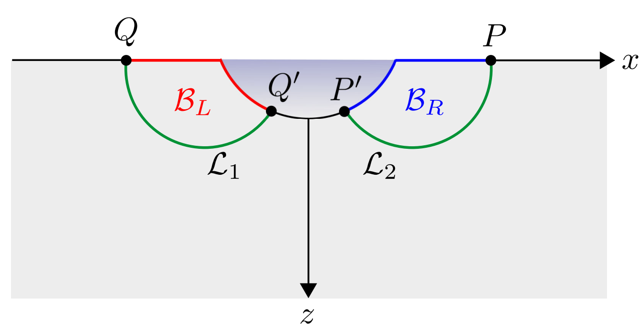

FIG. 14. Schematics of the defect extremal surface for the entanglement negativity between black hole interiors in the disconnected phase.

The coordinates of P' and Q' are obtained via extremizing the generalized entropy functional for $B_L \cup B_R$ which, in the (y, x) coordinates, are given by (τ_0, x_0) and $(\tau_0, -x_0)$ respectively [94]. Now employing the doubling trick [123,127], the correlation function in Eq. (5.24) may be expressed as a chiral four-point function on the full complex plane as

$$\langle \mathcal{T}_{n_e}(P')\bar{\mathcal{T}}_{n_e}(Q')\rangle_{\mathrm{BCFT}^{\otimes n_e}} = \langle \mathcal{T}_{n_e}(P')\bar{\mathcal{T}}_{n_e}(Q')\bar{\mathcal{T}}_{n_e}(Q'')\mathcal{T}_{n_e}(P'')\rangle_{\mathrm{CFT}^{\otimes n_e}}, \tag{5.25}$$

where P'': $(-\tau_0, x_0)$ and Q'': $(-\tau_0, -x_0)$ are the image points of P' and Q' upon reflection through the boundary at $\tau = 0$. The above four-point correlator is again factorized into two two-point functions in the dominant channel and similar to the previous subsection, the effective semiclassical entanglement negativity vanishes. Hence, the boundary QES result is reproduced through the bulk computations. Note that for this disconnected phase, we observe a perfect Markov recovery process as the bulk entanglement wedge is disconnected.

3. *Page curve*

From the results of the last two subsections, we may infer that the time evolution of the entanglement negativity between the black hole interiors is governed by the two phases of the extremal surfaces corresponding to the entanglement entropy of $B_L \cup B_R$. It is well-known that the unitary time evolution of the entanglement entropy for a subsystem in the Hawking radiation flux from a black hole is governed by the *Page curve* [7–9]. Hence the transition between the two different phases of the entanglement negativity between B_L and B_R occurs precisely at the Page time T_P, given by [63,94]

$$T_P = \cosh^{-1}\left(\sinh X_0\, e^{\tanh^{-1}(\sin\theta_0)} \frac{2\ell}{\epsilon_y \cos\theta_0}\right). \tag{5.26}$$

In the first phase the entanglement negativity is a decreasing function of the Rindler time given by Eq. (5.12). At the Page time T_P the extremal surface for the entanglement entropy transits to the disconnected phase and an entanglement entropy island corresponding to the radiation bath appears inside the gravitational regions on the EOW brane $\mathbb{Q}$. At this time, the entanglement negativity also transits to the corresponding disconnected phase and vanishes identically. The variation of the entanglement negativity between black hole interiors with the Rindler time T is plotted in Fig. 15.

C. Entanglement negativity between the black hole and the radiation

In this subsection, we now proceed to the computation of the entanglement negativity between the black hole region and the radiation region in the time-dependent scenario of defect $\mathrm{AdS}_3/\mathrm{BCFT}_2$ framework. To this end, we consider the black hole region to be described by a spacelike interval B_L on the left half of the two-sided eternal black hole and the radiation region to be described by a semi-infinite interval R_L adjacent to B_L as shown in Fig. 16. Similar to the previous case, there are two phases possible in this case which are investigated below.

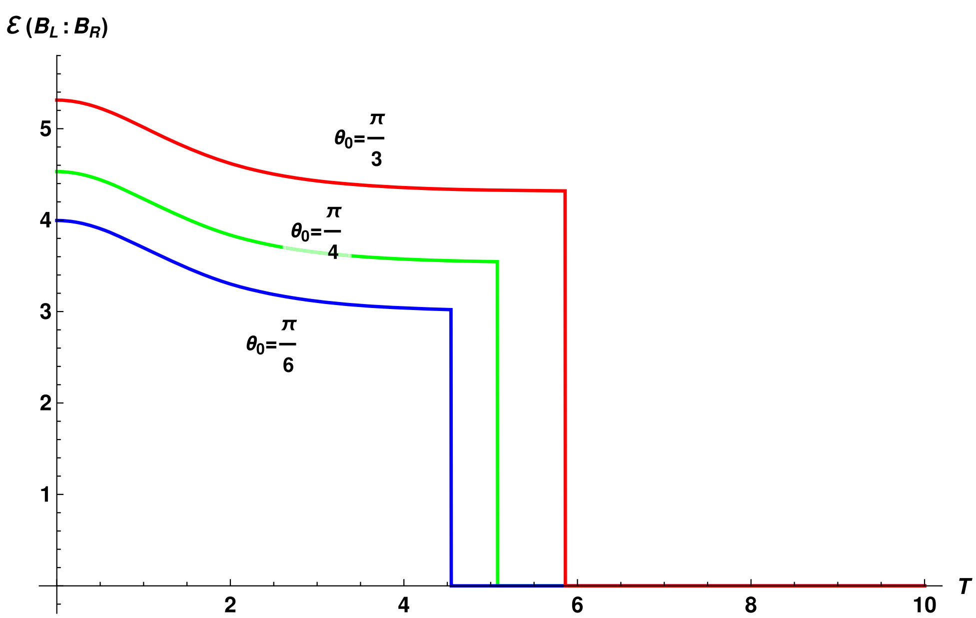

FIG. 15. The Page curve for entanglement negativity between black hole interiors for three different values of the EOW brane angle θ_0. Here the variation of the entanglement negativity with respect to the Rindler time T is shown in units of $\frac{c}{4}$ with $X_0 = 1$, $\epsilon_y = 0.1$, $\ell = 1$ and $\theta_0 = \frac{\pi}{3}, \frac{\pi}{4}, \frac{\pi}{6}$.

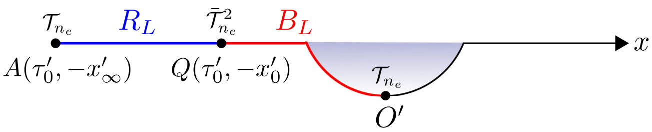

FIG. 16. Schematics of the defect extremal surface for the entanglement negativity between the black hole and the radiation in the connected phase.

1. Connected phase

The connected phase corresponds to the case where R_L does not posses an entanglement island and thus B_L covers the complete left black hole region on the EOW brane as shown in Fig. 16. From the doubly holographic perspective, this corresponds to an extremal surface for $R_L \cup B_L$ extending from the dynamical endpoint O' of B_L on the EOW brane to spatial infinity. We compute the entanglement negativity between the two adjacent intervals $B_L \equiv |O'Q|$ and $R_L \equiv |QA|$ in this phase where we have regularized the semi-infinite interval R_L to end at some point $A:(\tau_0', -x_\infty')$ which is later taken to infinity.

Boundary description. For the connected phase, the absence of the entanglement island for the radiation region R_L implies that the generalized entanglement negativity does not receive any area contribution in the $2d$ effective boundary description. The remaining effective semiclassical entanglement negativity between B_L and R_L may be computed through the following three-point twist correlator

$$\mathcal{E}^{\text{eff}}(B_L : R_L) = \lim_{n_e \to 1} \log[(\epsilon_y \Omega_{O'})^{\Delta_{n_e}} \langle \mathcal{T}_{n_e}(O') \bar{\mathcal{T}}^2_{n_e}(Q) \mathcal{T}_{n_e}(A) \rangle], \tag{5.27}$$

where ϵ_y is a UV cutoff on the dynamical EOW $\mathbb{Q}$ and $\Omega_{O'}$ is the warp factor as given in Eq. (5.6). In the unprimed coordinates, the points O' and Q are located at $(-y, 0)$ and $(\tau_0, -x_0)$, respectively. Using Eq. (5.2), we may locate the spatial infinity A in the unprimed coordinates at $(\tau, x) = (2, 0)$. Now, by utilizing the usual form of a CFT_2 three-point twist correlator given in Eq. (5.7), we may obtain the total generalized entanglement negativity in the boundary description for this case to be

$$\mathcal{E}^{\text{bdy}}_{\text{gen}} = \frac{c}{8}\left[\log \frac{((\tau_0 + y)^2 + x_0^2)(x_0^2 + (2 - \tau_0)^2)}{(y + 2)^2} - 2\log \frac{4\epsilon}{(\tau_0' + 1)^2 + x_0'^2}\right], \tag{5.28}$$

where ϵ is the UV cutoff in the primed coordinates. The above expression is then extremized over the position y of the dynamical point O' on the EOW brane to obtain

$$y = \frac{x_0^2}{2 - \tau_0} - \tau_0. \tag{5.29}$$

It may be checked through Eqs. (5.2) and (5.4) that $\tau < 2$ for the Rindler time $T > 0$ which guarantees the non-negativity of y for large x_0. We may now compute the entanglement negativity by substituting the above value of y in Eq. (5.28) to be

$$\mathcal{E}^{\text{bdy}} = \frac{c}{4}\log x_0 - \frac{c}{4}\log \frac{4\epsilon}{(\tau_0' + 1)^2 + x_0'^2}. \tag{5.30}$$

Transforming this result to the Rindler coordinates (X, T) through Eqs. (5.2) and (5.4), we may obtain the final expression for the entanglement negativity between the black hole region B_L and the radiation region R_L in the boundary description to be

$$\mathcal{E}^{\text{bdy}}(B_L : R_L) = \frac{c}{4}\log \frac{\cosh T}{\epsilon} + X_0, \tag{5.31}$$

where X_0 corresponds to the endpoint Q of the black hole region B_L at the fixed Rindler time T. We note here that the entanglement negativity in the above expression is an increasing function of the Rindler time T in this connected phase.

Bulk description. In the bulk description for this phase as depicted in Fig. 17, the generalized entanglement negativity between the black hole region $B_L \equiv |O'Q|$ and the radiation region $R_L \equiv |QA|$ is computed by employing the following formula

$$\begin{aligned}\mathcal{E}^{\text{bulk}}_{\text{gen}}(\mathcal{B}_L : \mathcal{R}_L) &= \frac{3}{16G_N}(\mathcal{L}_{R_L} + \mathcal{L}_{B_L} - \mathcal{L}_{B_L \cup R_L}) \\ &= \frac{c}{8}\left(\log \frac{[(\tau_0 + z\tan\theta_0)^2 + x_0^2 + z^2](x_0^2 + (2 - \tau_0)^2)}{[(2 + z\tan\theta_0)^2 + z^2]} - 2\log \frac{4\epsilon}{(\tau_0' + 1)^2 + x_0'^2}\right),\end{aligned} \tag{5.32}$$

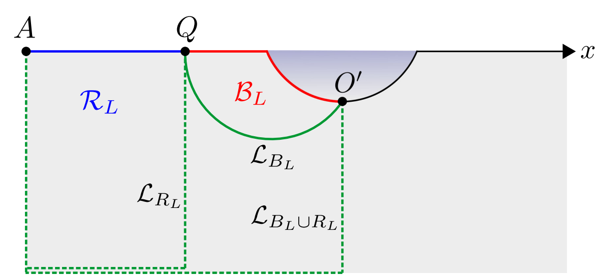

FIG. 17. Schematics of the defect extremal surface for the entanglement negativity between the black hole and the radiation in the connected phase.

where O': $(-z\tan\theta_0, 0, z)$ and Q: $(\tau_0, -x_0, 0)$ are the endpoints of B_L, and A: $(2, 0, 0)$ is the regularized endpoint of the semi infinite radiation region R_L in the unprimed coordinates. We have also used the Brown-Henneaux formula [170] in the second equality of the above expression. Note that the semiclassical effective entanglement negativity appearing as the second term in Eq. (3.4) vanishes in this case as R_L does not posses an entanglement island. We may extremize Eq. (5.32) over the position of the dynamical point O' to obtain

$$\partial_z \mathcal{E}^{\mathrm{bulk}}_{\mathrm{gen}} = 0 \Rightarrow z = \frac{x_0^2 \cot\theta_0}{2-\tau_0}, \tag{5.33}$$

where we have used the approximation that x_0 is large. The total entanglement negativity between the black hole region B_L and the radiation region R_L in the Rindler coordinates (X, T) for this phase may now be obtained by utilizing Eqs. (5.33), (5.32), (5.2), and (5.4) to be

$$\mathcal{E}^{\mathrm{bulk}}(\mathcal{B}_L: \mathcal{R}_L) = \frac{c}{4}\log\frac{\cosh T}{\epsilon} + X_0, \tag{5.34}$$

where X_0 corresponds to the point Q at the fixed Rindler time T. Remarkably, the above expression for the entanglement negativity matches exactly with the boundary description result in Eq. (5.31). We should also note here that the above result for the entanglement negativity is exactly same as the corresponding reflected entropy [63] and is consistent with the geometric interpretation of the Markov gap as the EWCS has trivial boundaries in this case.

2. Disconnected phase

The disconnected phase is described by the case where the semi-infinite radiation region R_L has an entanglement island labeled as $I_L \equiv |O'Q'|$ as depicted in Fig. 18. From the bulk perspective, this corresponds to an extremal surface for R_L to end on some point Q' on the EOW brane. The entanglement negativity between the black hole region B_L and the radiation region R_L for this case will thus receive contribution from the island region I_L on the EOW brane.

Boundary description. In the boundary description, the area contribution to the entanglement negativity corresponding

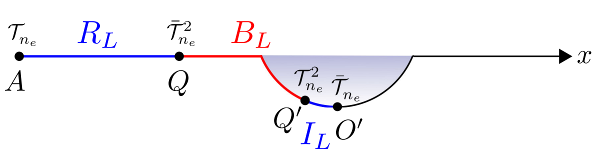

FIG. 18. Schematics of the defect extremal surface for the entanglement negativity between the black hole and the radiation in the disconnected phase.

to the point $Q' = \partial B_L \cap \partial I_L$ is as given in Eq. (2.8). The remaining effective semiclassical entanglement negativity between B_L and R_L may be computed through the following four-point twist correlator,

$$\begin{aligned}\mathcal{E}^{\mathrm{eff}}(B_L: R_L \cup I_L) &= \lim_{n_e\to 1}\log[(\epsilon_y\Omega_{Q'})^{\Delta^{(2)}_{n_e}}(\epsilon_y\Omega_{O'})^{\Delta_{n_e}} \\ &\quad\times\langle\mathcal{T}_{n_e}(A)\bar{\mathcal{T}}^2_{n_e}(Q)\mathcal{T}^2_{n_e}(Q')\bar{\mathcal{T}}_{n_e}(O')\rangle],\end{aligned} \tag{5.35}$$

where Ω are the warp factors as given in Eq. (5.6), A is the regularized endpoint of the semi-infinite interval R_L and the point Q' and Q are at position $(-y, -x)$ and $(\tau_0, -x_0)$, respectively in the unprimed coordinates. For the bipartite configuration under consideration, the above four-point twist correlator factorizes into two two-point twist correlators in the following way:

$$\begin{aligned}&\langle\mathcal{T}_{n_e}(A)\bar{\mathcal{T}}^2_{n_e}(Q)\mathcal{T}^2_{n_e}(Q')\bar{\mathcal{T}}_{n_e}(O')\rangle \\ &\quad\approx\langle\mathcal{T}_{n_e}(A)\bar{\mathcal{T}}_{n_e}(O')\rangle\rangle\langle\bar{\mathcal{T}}^2_{n_e}(Q)\mathcal{T}^2_{n_e}(Q')\rangle.\end{aligned} \tag{5.36}$$

Utilizing the above factorization in Eq. (5.35) along with the area term in Eq. (2.8), the generalized entanglement negativity for this case may be expressed as

$$\begin{aligned}\mathcal{E}^{\mathrm{bdy}}_{\mathrm{gen}} = \frac{c}{4}\Bigg(&\tanh^{-1}(\sin\theta_0) + \log\frac{\ell}{\epsilon_y y\cos\theta_0} \\ &+\log((y+\tau_0)^2 + (x-x_0)^2) \\ &-\log\frac{4\epsilon}{(\tau_0'+1)^2 + x_0'^2}\Bigg),\end{aligned} \tag{5.37}$$

where again ϵ is the UV cutoff in the primed coordinates. Interestingly, the regularized point A does not enter the computation in this case. We may now extremize the above generalized entanglement negativity over the position of the dynamical point Q' i.e., $\partial_y\mathcal{E}^{\mathrm{bdy}}_{\mathrm{gen}} = 0$ and $\partial_x\mathcal{E}^{\mathrm{bdy}}_{\mathrm{gen}} = 0$ to obtain

$$y = \tau_0, \qquad x = x_0. \tag{5.38}$$

Using the above values of the coordinates y and x in Eq. (5.37) and transforming the result to the primed coordinates Eq. (5.2) and subsequently to the Rindler coordinates (5.4) via the analytic continuation $\tau = it'$, we may obtain the total entanglement negativity between the black hole region B_L and the radiation region R_L to be

$$\begin{aligned}&\mathcal{E}^{\mathrm{bdy}}(B_L: R_L) \\ &\quad= \frac{c}{4}\left(\tanh^{-1}(\sin\theta_0) + \log\frac{e^{2X_0}-1}{\epsilon} + \log\frac{2\ell}{\epsilon_y\cos\theta_0}\right).\end{aligned} \tag{5.39}$$

Here X_0 corresponds to the endpoint Q of the black hole region B_L. Note that the above expression for the entanglement negativity is independent of the Rindler time T and only depends on the position of the point Q.

Bulk description. In the $3d$ bulk description for the disconnected phase, the entanglement negativity between the black hole region B_L and the radiation region R_L is computed by employing the DES formula in Eq. (3.4) as follows:

$$\begin{aligned}\mathcal{E}^{\text{bulk}}_{\text{gen}}(\mathcal{B}_L:\mathcal{R}_L) &= \frac{3}{16G_N}(\mathcal{L}_{B_L}+\mathcal{L}_{R_L}-\mathcal{L}_{B_L\cup R_L})\\ &\quad+\mathcal{E}^{\text{eff}}(\mathcal{B}_L:\mathcal{R}_L)\\ &= \frac{3}{8G_N}\mathcal{L}_2+\mathcal{E}^{\text{eff}}(B_L:I_L),\end{aligned} \tag{5.40}$$

where $\mathcal{L}_2$ is the extremal curve between points Q': $(-z\tan\theta_0,-x_1,z)$ and Q:$(\tau_0,-x_0,0)$ and I_L is the island region corresponding to the radiation region R_L as depicted in Fig. 19. In the second term of the above expression we have also utilized the fact that bulk matter fields are only localized on the EOW brane $\mathbb{Q}$. We note here that, consistent with the boundary description, the regularized point A does not enter the computation in this phase. The length of the extremal curve $\mathcal{L}_2$ in the unprimed coordinates may be expressed as [10,11]

$$\begin{aligned}\mathcal{L}_2 &\equiv \mathcal{L}_{QQ'}\\ &= \ell\,\log\left[\frac{(\tau_0+z\tan\theta_0)^2+(x_0-x_1)^2+z^2}{z}\right]\\ &\quad-\ell\,\log\left(\frac{4\epsilon}{(\tau_0'+1)^2+x_0'^2}\right).\end{aligned} \tag{5.41}$$

The semiclassical effective entanglement negativity appearing as the last term in Eq. (5.40) may be obtained to be

$$\mathcal{E}^{\text{eff}}(B_L:I_L)=\frac{c}{4}\log\frac{2\ell}{\epsilon_y\cos\theta_0}, \tag{5.42}$$

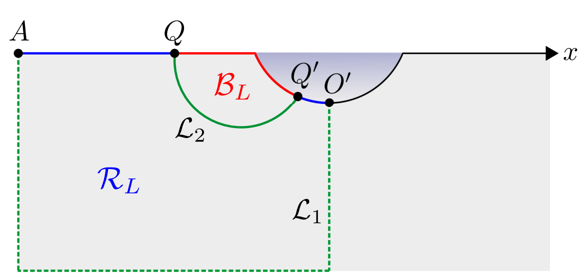

FIG. 19. Schematics of the defect extremal surface for the entanglement negativity between the black hole and the radiation in the disconnected phase.

where ϵ_y is the UV cutoff on the dynamical EOW brane. Extremizing the generalized entanglement negativity obtained by substituting Eqs. (5.41) and (5.42) in Eq. (5.40), with respect to the position of Q' i.e., $\partial_z\mathcal{E}^{\text{bulk}}_{\text{gen}}=0$ and $\partial_{x_1}\mathcal{E}^{\text{bulk}}_{\text{gen}}=0$, we may obtain

$$z=\tau_0\cos\theta_0,\qquad x_1=x_0. \tag{5.43}$$

The total entanglement negativity between the black hole region B_L and the radiation region R_L in the primed coordinates may then be obtained through Eqs. (5.43) and (5.2) to be

$$\begin{aligned}\mathcal{E}^{\text{bulk}}(\mathcal{B}_L:\mathcal{R}_L) &= \frac{c}{4}\left[\log\left(\frac{x_0'^2+\tau_0'^2-1}{\epsilon}\right)+\tanh^{-1}(\sin\theta_0)\right.\\ &\quad\left.+\log\left(\frac{2\ell}{\epsilon_y\cos\theta_0}\right)\right],\end{aligned} \tag{5.44}$$

where the Brown-Henneaux formula [170] has been used. On transformation to the Rindler coordinates Eq. (5.4) via the analytic continuation $\tau'=it'$, the above expression matches exactly with the boundary perspective result in Eq. (5.39) which serves as a strong consistency check for our proposals. Once again we note that the above result consistently match with the corresponding reflected entropy [63] as the Markov gap is vanishing for this configuration.

3. Page curve

We now analyze the results of the last two subsections where we have computed the entanglement negativity between the black hole region B_L and the radiation region R_L for the two possible phases. In the connected phase, the entanglement negativity computed in Eq. (5.31) is an increasing function of the Rindler time T. In contrast, for the disconnected phase, the entanglement negativity given in Eq. (5.39) is independent of T and only depends on the size of the black hole region B_L. A transition from the connected phase to the disconnected phase is observed at the Page time for the entanglement entropy given in Eq. (5.26). In Fig. 20, we show the variation of the time dependent entanglement negativity between the black hole region B_L and the radiation R_L with the Rindler time T for three different values of the EOW brane angle θ_0.

D. Entanglement negativity between subsystems in the radiation bath

In this subsection, we compute the entanglement negativity between the right-subsystem R_R and the left-subsystem R_L in the radiation region as shown in Fig. 21. In the Rindler coordinates (X,T), the right-radiation subsystem R_R extends from (X_0,T) to (X_1,T) and the left-radiation subsystem R_L extends from $(X_0,-T+i\pi)$ to $(X_1,-T+i\pi)$. In the primed coordinates, the subsystems $R_R\equiv|NQ|$ and

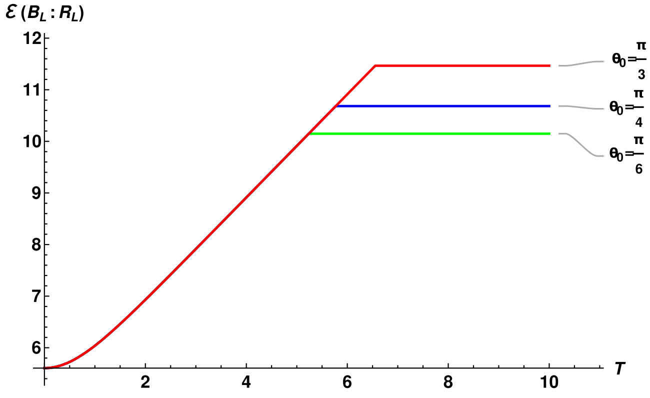

FIG. 20. The Page curve for the entanglement negativity between the black hole region and the radiation region for three different values of the EOW brane angle θ_0. Here the variation of the entanglement negativity with respect to the Rindler time T is shown in units of $\frac{c}{4}$ with $X_0 = 1$, $\epsilon = 0.01$, $\epsilon_y = 0.1$, $\ell = 1$ and $\theta_0 = \frac{\pi}{3}, \frac{\pi}{4}, \frac{\pi}{6}$.

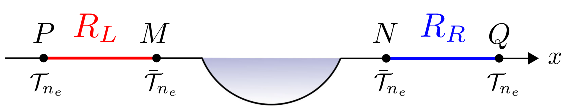

FIG. 21. Schematics of the quantum extremal surface for the entanglement negativity between intervals in the radiation region in the connected phase.

$R_L \equiv |PM|$ are mapped to the intervals $[(\tau'_0, x'_0), (\tau'_1, x'_1)]$ and $[(\tau'_1, -x'_1), (\tau'_0, -x'_0)]$, respectively. Similar to the earlier subsections, we perform the computation in the Euclidean signature and subsequently transform the results to Rindler coordinates in the Lorentzian signature. Depending on the phase transition of the extremal surfaces corresponding to $R_L \cup R_R$, the DES corresponding to the entanglement negativity between them crosses from a connected phase to a disconnected phase. In the following, we investigate the time evolution of the entanglement negativity between R_L and R_R from both the bulk and the boundary perspective.

1. Connected phase

In the connected phase, there are no entanglement entropy islands corresponding to R_L and R_R in the effective boundary description as illustrated in Fig. 21. In this phase, we compute the entanglement negativity between the disjoint radiation subsystems R_L and R_R.

Boundary description. As there are no island contributions in this phase, we observe from Eq. (3.2) that the entanglement negativity between the radiation subsystems in $2d$ effective boundary description reduces to the effective entanglement negativity between two disjoint intervals as follows:

$$\begin{aligned}\mathcal{E}^{\mathrm{bdy}}(R_L :\, R_R) &= \mathcal{E}^{\mathrm{eff}}(R_L : R_R)\\ &= \lim_{n_e\to 1} \log[\langle \mathcal{T}_{n_e}(P)\bar{\mathcal{T}}_{n_e}(M)\bar{\mathcal{T}}_{n_e}(N)\mathcal{T}_{n_e}(Q)\rangle_{\mathrm{CFT}^{\otimes n_e}}].\end{aligned} \tag{5.45}$$

As described in Sec. IVA 2, for the two disjoint subsystems in the t-channel, the above four-point twist correlator may be computed in the large central-charge limit as follows [151]:

$$\begin{aligned}\mathcal{E}^{\mathrm{bdy}}(R_L : R_R) &= \frac{c}{4}\log\left(\frac{|PN||MQ|}{|MN||PQ|}\right)\\ &= \frac{c}{4}\log\frac{(e^{X_0}+e^{X_1})^2 - (e^{X_0}-e^{X_1})^2\tanh^2 T}{4e^{X_0+X_1}}.\end{aligned} \tag{5.46}$$

Note that the entanglement negativity between the radiation subsystems R_L and R_R is a monotonically decreasing function of the Rindler time T in this phase.

Bulk description. In the $3d$ bulk description, the effective entanglement negativity in Eq. (3.3) vanishes as the corresponding entanglement wedges contain no quantum matter fields as illustrated in Fig. 22. The entanglement negativity between R_L and R_R is then given entirely by the combination of the lengths of the defect extremal surfaces as follows:

$$\begin{aligned}\mathcal{E}^{\mathrm{bulk}}(\mathcal{R}_L :\, \mathcal{R}_R) &= \frac{3}{16G_N}(\mathcal{L}_{PN}+\mathcal{L}_{MQ}-\mathcal{L}_{MN}-\mathcal{L}_{PQ})\\ &= \frac{3\ell}{8G_N}\left[\log\left(\frac{(x'_1+x'_0)^2+(\tau'_1-\tau'_0)^2}{\epsilon^2}\right)\right.\\ &\quad\left. -\log\left(\frac{2x'_0}{\epsilon}\right)-\log\left(\frac{2x'_1}{\epsilon}\right)\right],\end{aligned} \tag{5.47}$$

where we have used the fact that the length of an extremal curve $\mathcal{L}_{ab}$ connecting two points (τ'_a, x'_a) and (τ'_b, x'_b) on the boundary is given by [11]

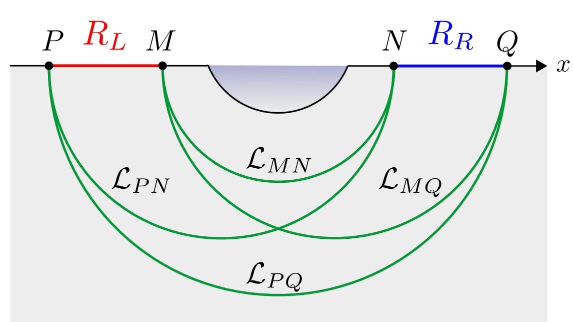

FIG. 22. Schematics of the defect extremal surface for the entanglement negativity between intervals in the radiation region in the connected phase.

$$\mathcal{L}_{ab} = \ell \log\left[\frac{(x'_a - x'_b)^2 + (\tau'_a - \tau'_b)^2}{\epsilon^2}\right]. \quad (5.48)$$

Now analytically continuing to the Lorentzian signature and transforming to the Rindler coordinates in Eq. (5.4), we obtain the entanglement negativity between R_L and R_R in the bulk description to be

$$\mathcal{E}^{\mathrm{bulk}}(\mathcal{R}_L : \mathcal{R}_R) = \frac{c}{4}\log\frac{(e^{X_0} + e^{X_1})^2 - (e^{X_0} - e^{X_1})^2\tanh^2 T}{4e^{X_0+X_1}}, \quad (5.49)$$

which matches exactly with the result from the boundary description, given in Eq. (5.46). Note that in the limit of large X_1 where the two disjoint intervals R_L and R_R are in proximity, the above expression reduces to

$$\mathcal{E}^{\mathrm{bulk}}(\mathcal{R}_L : \mathcal{R}_R) = \frac{c}{4}(X_1 - X_0 - 2\log(\cosh T)) - \frac{c}{4}\log 4. \quad (5.50)$$

The last term in the above expression describes the geometric Markov gap as compared to the corresponding reflected entropy [63].

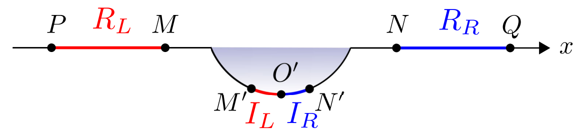

FIG. 23. Schematics of the quantum extremal surface for the entanglement negativity between intervals in the radiation region in the disconnected phase. I_L and I_R denote the entanglement negativity islands corresponding to R_L and R_R, respectively.

2. Disconnected phase

For the disconnected phase, the entanglement entropy corresponding to the radiation subsystems receives island contributions as depicted in Fig. 23. The entanglement negativity islands corresponding to the radiation subsystems R_L and R_R, located on the EOW brane, are denoted as $I_L \equiv |M'O'|$ and $I_R \equiv |O'N'|$, respectively.[15] We now proceed to compute the entanglement negativity between the radiation subsystems in the boundary and bulk descriptions in this phase.

Boundary description. In the $2d$ boundary perspective, the area term corresponding to the point $O' = \partial I_L \cap \partial I_R$ is a constant given by Eq. (2.8). The remaining effective semiclassical entanglement negativity in Eq. (3.2) may be expressed as

$$\begin{aligned}\mathcal{E}^{\mathrm{eff}}&(R_L \cup I_L : R_R \cup I_R) \\ &= \lim_{n_e \to 1} \log[(\epsilon_y \Omega_{M'})^{\Delta_{n_e}} (\epsilon_y \Omega_{N'})^{\Delta_{n_e}} (\epsilon_y \Omega_{O'})^{\Delta^{(2)}_{n_e}} \langle \mathcal{T}_{n_e}(P)\bar{\mathcal{T}}_{n_e}(M)\mathcal{T}_{n_e}(M')\bar{\mathcal{T}}^2_{n_e}(O')\mathcal{T}_{n_e}(N')\bar{\mathcal{T}}_{n_e}(N)\mathcal{T}_{n_e}(Q)\rangle_{n_e}]. \quad (5.51)\end{aligned}$$

In the large central-charge limit, the above twist correlator may be factorized in the dominant channel as follows:[16]

$$\langle \bar{\mathcal{T}}_{n_e}(M)\mathcal{T}_{n_e}(M')\rangle \langle \mathcal{T}_{n_e}(P)\bar{\mathcal{T}}^2_{n_e}(O')\mathcal{T}_{n_e}(Q)\rangle \times \langle \mathcal{T}_{n_e}(N')\bar{\mathcal{T}}_{n_e}(N)\rangle. \quad (5.52)$$

Now, employing the replica limit $n_e \to 1$, the effective semiclassical entanglement negativity Eq. (5.51) in the disconnected phase reduces to

$$\begin{aligned}\mathcal{E}^{\mathrm{eff}}&(R_L \cup I_L : R_R \cup I_R) \\ &\approx \lim_{n_e \to 1} \log\left[(\epsilon_y \Omega_{O'})^{\Delta^{(2)}_{n_e}} \langle \mathcal{T}_{n_e}(P)\bar{\mathcal{T}}^2_{n_e}(O')\mathcal{T}_{n_e}(Q)\rangle\right] \\ &= \frac{c}{4}\log\left(\frac{\ell}{\epsilon_y y \cos\theta_0}\right) + \frac{c}{4}\log\left[\frac{(y+\tau_1)^2 + x_1^2}{2x_1}\right], \quad (5.53)\end{aligned}$$

where the coordinates for P, Q and O' are given by $(\tau_1, -x_1)$, (τ_1, x_1) and $(-y, 0)$ respectively. The generalized entanglement negativity between R_L and R_R in the $2d$ boundary description may now be obtained using Eqs. (5.53) and (3.2) as follows:

$$\begin{aligned}\mathcal{E}^{\mathrm{bdy}}_{\mathrm{gen}}(R_L : R_R) = &\frac{c}{4}\log\left(\frac{\ell}{\epsilon_y y \cos\theta_0}\right) + \frac{c}{4}\log\left[\frac{(y+\tau_1)^2 + x_1^2}{2x_1}\right] \\ &+ \frac{c}{4}\tanh^{-1}(\sin\theta_0). \quad (5.54)\end{aligned}$$

Extremizing the above generalized entanglement negativity with respect to y we obtain

$$\partial_y \mathcal{E}^{\mathrm{bdy}}_{\mathrm{gen}}(R_L : R_R) = 0 \Rightarrow y = \sqrt{\tau_1^2 + x_1^2}. \quad (5.55)$$

Now, substituting the value of y in Eq. (5.54), the entanglement negativity between the radiation subsystems for the disconnected phase in the boundary description is given by

[15] Note that the entanglement negativity islands together constitute the entanglement entropy island for $R_L \cup R_R$.

[16] The correlators are factorized into their respective contractions as depicted by the choice of the extremal surfaces in Fig. 24.

$$\mathcal{E}^{\rm bdy}(R_L:R_R)=\frac{c}{4}\left[\log\frac{\sqrt{\tau_1^2+x_1^2}+\tau_1}{x_1}+\log\left(\frac{\ell}{\epsilon_y\cos\theta_0}\right)+\tanh^{-1}(\sin\theta_0)\right]. \tag{5.56}$$

Finally, transforming to the primed coordinates in Eq. (5.2), performing the Lorentzian continuation and utilizing Eq. (5.4) we obtain the entanglement negativity between the radiation subsystems in terms of the Rindler coordinates (X,T) in the $2d$ effective boundary description as follows:

$$\mathcal{E}^{\rm bdy}(R_L:R_R)=\frac{c}{4}\left[\log\frac{e^{2X_1}-1+\sqrt{4e^{2X_1}\cosh^2T+(e^{2X_1}-1)^2}}{2e^{X_1}\cosh T}+\log\left(\frac{\ell}{\epsilon_y\cos\theta_0}\right)+\log\left(\frac{\cos\theta_0}{1-\sin\theta_0}\right)\right]. \tag{5.57}$$

Bulk description. In the disconnected phase, due to the presence of entanglement islands, a portion of the EOW brane $\mathbb{Q}$ is contained within the entanglement wedge of the radiation in the $3d$ bulk description. As depicted in Fig. 24, $|M'N'|$ denotes the entanglement entropy island corresponding to $R_L\cup R_R$. The bulk EWCS ends on the EOW brane at the point O' and splits the entanglement wedge corresponding to $R_L\cup R_R$ into two codimension-one regions $\mathcal{R}_L$ and $\mathcal{R}_R$, respectively. For this phase, the entanglement negativity between R_L and R_R corresponds to the configuration of disjoint subsystems $|PM|\cup|O'M'|$ and $|NQ|\cup|O'N'|$, sandwiching the region $|MM'|\cup|NN'|$ in between. Therefore, we may employ the DES formula in Eq. (3.3) to obtain

$$\begin{aligned}\mathcal{E}^{\rm bulk}_{\rm gen}(\mathcal{R}_L:\mathcal{R}_R)&=\frac{3}{16G_N}[(\mathcal{L}_1+\mathcal{L}_4)+(\mathcal{L}_2+\mathcal{L}_3)\\&\quad-(\mathcal{L}_3+\mathcal{L}_4)-\mathcal{L}_5]+\mathcal{E}^{\rm eff}(\mathcal{R}_L:\mathcal{R}_R)\\&=\frac{3}{16G_N}(\mathcal{L}_1+\mathcal{L}_2-\mathcal{L}_5)+\mathcal{E}^{\rm eff}(I_L:I_R),\end{aligned} \tag{5.58}$$

where as earlier, the effective entanglement negativity between bulk matter fields reduces to that between the adjacent intervals $I_L\equiv|O'M'|$ and $I_R\equiv|O'N'|$ on the EOW brane. The lengths of the extremal surfaces in Eq. (5.58) are given by [10,11,94]

$$\begin{aligned}\mathcal{L}_1&=\ell\,\log\left[\frac{(\tau_1+z\tan\theta_0)^2+x_1^2+z^2}{z}\right]\\&\quad-\ell\,\log\left[\frac{4\epsilon}{(\tau_1'+1)^2+x_1'^2}\right]=\mathcal{L}_2,\\\mathcal{L}_5&=2\ell\,\log(2x_1)-2\ell\,\log\left[\frac{4\epsilon}{(\tau_1'+1)^2+x_1'^2}\right],\end{aligned} \tag{5.59}$$

where the second logarithmic term corresponds to the UV cutoff in the unprimed coordinates [63,94]. The effective entanglement negativity in Eq. (5.58) between the island regions I_L and I_R may be computed through a three-point correlator of twist fields inserted at the endpoints of the intervals as follows:

$$\begin{aligned}\mathcal{E}^{\rm eff}(I_L:I_R)=&\lim_{n_e\to1}\log[(\epsilon_y^2\Omega_{M'}\Omega_{N'})^{\Delta_{n_e}}(\epsilon_y\Omega_{O'})^{\Delta^{(2)}_{n_e}}\\&\times\langle\mathcal{T}_{n_e}(M')\bar{\mathcal{T}}^2_{n_e}(O')\mathcal{T}_{n_e}(N')\rangle_{\rm BCFT^{\otimes n_e}}].\end{aligned} \tag{5.60}$$

The above three-point twist correlator on the half plane describing the BCFT may be expressed as a six-point correlator of chiral twist fields on the whole complex plane using the doubling trick [123,127] as follows:

$$\begin{aligned}&\langle\mathcal{T}_{n_e}(M')\bar{\mathcal{T}}^2_{n_e}(O')\mathcal{T}_{n_e}(N')\rangle_{\rm BCFT^{\otimes n_e}}\\&=\langle\mathcal{T}_{n_e}(M')\bar{\mathcal{T}}_{n_e}(M)\bar{\mathcal{T}}^2_{n_e}(O')\mathcal{T}^2_{n_e}(O)\mathcal{T}_{n_e}(N')\bar{\mathcal{T}}_{n_e}(N')\rangle_{\rm CFT^{\otimes n_e}},\end{aligned} \tag{5.61}$$

where M, N and O are the image of the points M', N' and O' on the EOW brane respectively. In the large central-charge limit, the six-point correlator may be further factorized in the dominant channel similar to Eq. (5.52) as follows:

$$\langle\bar{\mathcal{T}}_{n_e}(M)\mathcal{T}_{n_e}(M')\rangle\langle\bar{\mathcal{T}}^2_{n_e}(O')\mathcal{T}^2_{n_e}(A)\rangle\langle\mathcal{T}_{n_e}(N')\bar{\mathcal{T}}_{n_e}(N)\rangle. \tag{5.62}$$

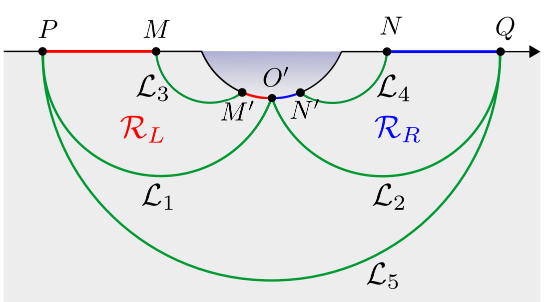

FIG. 24. Schematics of the defect extremal surface for the entanglement negativity between intervals in the radiation region in the disconnected phase.

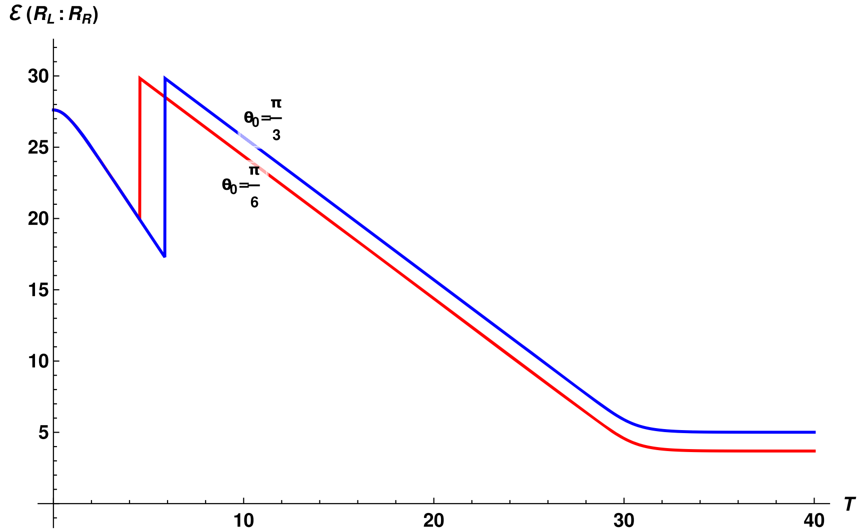

FIG. 25. The Page curve for entanglement negativity between the radiation and the radiation with respect to the Rindler time T in units of $\frac{c}{4}$. Here we choose $X_0 = 1$, $X_1 = 30$, $\epsilon_y = 0.1$, $\ell = 1$ and $\theta_0 = \frac{\pi}{3}, \frac{\pi}{6}$.

Now, reversing the doubling trick and subsequently employing the replica limit $n_e \to 1$, we may obtain the effective entanglement negativity between I_L and I_R as

$$\mathcal{E}^{\text{eff}}(I_L:\, I_R) = \lim_{n_e\to 1} \log\left[(\epsilon_y \Omega_{O'})^{\Delta^{(2)}_{n_e}} \langle \bar{\mathcal{T}}^2_{n_e}(O')\rangle_{\text{BCFT}^{\otimes n_e}}\right]$$
$$= \frac{c}{4}\log\frac{2\ell}{\epsilon_y \cos\theta_0}. \tag{5.63}$$

We may obtain the generalized entanglement negativity by substituting Eqs. (5.59) and (5.63) in Eq. (5.58) to be

$$\mathcal{E}^{\text{bulk}}_{\text{gen}}(\mathcal{R}_L:\mathcal{R}_R) = \frac{c}{4}\left[\log\left(\frac{(\tau_1 + z\tan\theta_0)^2 + x_1^2 + z^2}{2x_1 z}\right)\right.$$
$$\left. + \log\left(\frac{2\ell}{\epsilon_y \cos\theta_0}\right)\right], \tag{5.64}$$

where we have used the Brown-Henneaux formula [170] in the first term. The location of the dynamical point O' in the above expression is fixed through extremization at

$$z = \sqrt{\tau_1^2 + x_1^2}\cos\theta_0. \tag{5.65}$$

Substituting the above value of z in Eq. (5.64) and subsequently transforming the result to the Rindler coordinates using Eqs. (5.2) and (5.4), we may obtain the entanglement negativity between the radiation subsystems R_L and R_R to be

$$\mathcal{E}^{\text{bulk}}(\mathcal{R}_L:\,\mathcal{R}_R)$$
$$= \frac{c}{4}\left[\log\frac{e^{2X_1} - 1 + \sqrt{4e^{2X_1}\cosh^2 T + (e^{2X_1}-1)^2}}{2e^{X_1}\cosh T}\right.$$
$$\left. + \log\left(\frac{\ell}{\epsilon_y\cos\theta_0}\right) + \log\left(\frac{\cos\theta_0}{1-\sin\theta_0}\right)\right]. \tag{5.66}$$

We again observe that the above result in the bulk description matches exactly with the entanglement negativity from the boundary description in Eq. (5.57) for the disconnected phase. Also note that the above expression for the entanglement negativity differs from the corresponding reflected entropy by a constant amount given by $\frac{c}{4}\log 2$ which is consistent with the geometric interpretation of the Markov gap as discussed in Sec. II D.

3. Page curve

We now analyze the behavior of the time-dependent entanglement negativity between radiation subsystems as discussed in last two subsections. We observe that the entanglement negativity decreases with the Rindler time T in both phases and eventually plateaus out. In the limit when both the radiation subsystems R_L and R_R extends to spatial infinity, namely $X_1 \to \infty$, the asymptotic behavior of the entanglement negativity is given as

$$\mathcal{E}^{\text{bulk}}(\mathcal{R}_L:\mathcal{R}_R)$$
$$= \begin{cases} \frac{c}{4}(X_1 - X_0 - 2\log(2\cosh T)) & T < T_P \\ \frac{c}{4}\left(X_1 - \log\cosh T + \log\frac{\cos\theta_0}{1-\sin\theta_0} + \log\frac{\ell}{\epsilon_y\cos\theta_0}\right) & T > T_P, \end{cases} \tag{5.67}$$

where T_P is the Page time for the entanglement entropy as given in Eq. (5.26). Hence, the entanglement negativity shows a sudden jump at T_P, and in the limit $X_1 \to \infty$ this jump is given by

$$\Delta\mathcal{E} = \frac{c}{4}\left[2\log\left(\frac{2\ell}{\epsilon_y\cos\theta_0}\right) + 2\log\left(\frac{\cos\theta_0}{1-\sin\theta_0}\right) + \log(e^{2X_0}-1)\right]. \tag{5.68}$$

Note that this jump in the entanglement negativity differs from a similar jump observed in the context of the reflected entropy [63] by a constant $\frac{c}{4}\log 2$ which arises due to unequal Markov gap between the connected and the disconnected phase. The analog of the Page curve for the entanglement negativity for this bipartite configuration is shown in Fig. 25.

VI. SUMMARY AND DISCUSSION

To summarize, in this article, we have proposed a defect extremal surface prescription for the entanglement negativity of bipartite mixed-state configurations in the $\mathrm{AdS}_3/\mathrm{BCFT}_2$ scenarios which include defect conformal matter on the EOW brane. Furthermore, we have extended the island formula for the entanglement negativity to the framework of the defect $\mathrm{AdS}_3/\mathrm{BCFT}_2$, utilizing the lower dimensional effective description involving a CFT_2 coupled to semiclassical gravity. Interestingly, the bulk DES formula may be understood as the doubly holographic counterpart of the island formula for the entanglement negativity.

To begin with, we computed the entanglement negativity in the time independent scenarios involving adjacent and disjoint intervals on a static time slice of the conformal boundary of the $3d$ braneworld. To this end, we have demonstrated that the entanglement negativity for various bipartite states obtained through the DES formula matches exactly with the results from the corresponding QES prescription involving entanglement negativity islands. Subsequently we obtained the entanglement negativity in various time-dependent scenarios involving an eternal black hole coupled to a radiation bath in the effective lower-dimensional picture. In such time-dependent scenarios, we have obtained the entanglement negativity between subsystems in the black hole interior, between subsystems involving black hole and the radiation bath, and between subsystems in the radiation bath utilizing the island as well as the bulk DES formulas. In this connection, we have studied the time evolution of the entanglement negativity for the above configurations and obtained the analogs of the Page curves. Interestingly, the transitions between different phases of the defect extremal surfaces corresponding to the entanglement negativity for the above configurations occur precisely at the Page time for the corresponding entanglement entropy. Remarkably, it was observed that the entanglement negativity from the boundary and bulk proposals are in perfect agreement for the time-dependent cases, thus demonstrating the equivalence of both formulations. This serves as a strong consistency check for our proposals.

We would like to emphasize that the entanglement negativity for a bipartite mixed state is characterized by the reduced density matrix ρ_{AB} which in the bulk description corresponds to the entanglement wedge of $A \cup B$. Therefore, a prescription for the bulk construction for the entanglement negativity should naturally involve the complete entanglement wedge of $A \cup B$ and its subsequent bipartition. In this work, we propose obtaining this bipartition via the entanglement wedge cross section. The application of our proposal for all the cases considered in this article matches with the corresponding QES results at leading order in c. However, a nontrivial cross-check for the uniqueness of our proposal will possibly require the addition of quantum matter fields situated in the interior of the spacetime in addition to the matter fields located on the brane. We expect the results to differ only at the sub-leading orders in c for any alternate choice of the bulk regions $\mathcal{A}$ and $\mathcal{B}$. It is an interesting but nontrivial issue to check this by the explicit computations and is left for the future.[17]

There are several possible future directions to investigate. One such issue would be the extension of our proposals to higher-dimensional defect AdS/BCFT scenarios. One may also generalize our doubly holographic formulation for the entanglement negativity with the defect brane at a constant tension to arbitrary embeddings of the brane in the $3d$ bulk geometry. Furthermore, it would also be interesting to derive the bulk DES formula for the entanglement negativity through the gravitational path integral techniques utilizing the replica symmetry breaking wormhole saddles. We leave these open issues for future investigations.

ACKNOWLEDGMENTS

The work of G. S. is partially supported by the Dr. Jagmohan Garg Chair Professor position at the Indian Institute of Technology, Kanpur.

APPENDIX: ISLANDS FOR ENTANGLEMENT NEGATIVITY THROUGH THE ALTERNATIVE PROPOSAL

In this appendix we will investigate the entanglement negativity for various bipartite mixed states in the lower-dimensional effective picture through the alternative proposal involving Rényi reflected entropy of order one half described in [160,164] and briefly reviewed in Sec. II D. To proceed, we recall that the QES formula for the Rényi reflected entropy of order one half between two subsystems A and B may be written as [27,164]

[17]We thank the anonymous referee for raising this crucial point.

$$S_R^{(1/2)}(A:B) = \min_{\Gamma_R} \mathrm{Ext} \left[\frac{\mathcal{A}^{(1/2)}(\Gamma_R)}{2G_N} + S_{R\,\mathrm{eff}}^{(1/2)}(A \cup I_R(A) : B \cup I_R(B)) \right], \tag{A1}$$

where $I_R(A)$ and $I_R(B)$ denote the reflected entropy islands for A and B respectively, and the extremization is performed over the reflected entropy island cross section $\Gamma_R = \partial I_R(A) \cap \partial I_R(B)$. Furthermore, as described in [164], the order one half area contribution from the island cross section Γ_R may be rewritten as follows [cf. Eq. (4.17)]:

$$\mathcal{A}^{(1/2)}(\Gamma_R) = \frac{3}{2}\mathcal{A}(\Gamma_R) = \frac{3\ell}{8G_N} \tanh^{-1}(\sin\theta_0). \tag{A2}$$

In the following, we will compute the Rényi reflected entropy of order one half for various bipartite mixed states involving two disjoint and two adjacent intervals on a static time slice in the defect $\mathrm{AdS}_3/\mathrm{BCFT}_2$ model. Subsequently, we will compute the entanglement negativity for such bipartite states by utilizing the alternative proposal in Eq. (2.14) and comment on the corresponding Markov gaps.

1. Two disjoint intervals

We consider two disjoint intervals $A = [b_1, b_2]$ and $B = [b_3, \infty]$ in the bath CFT_2 coupled to the gravity theory on the EOW brane $\mathbb{Q}$. Similar to the discussion of the entanglement negativity in Sec. IV A, there are three possible phases for the Rényi reflected entropy.

a. Phase-I

When the two disjoint intervals A and B are far apart, there is no nontrivial island cross section for reflected entropy and the area term in Eq. (A1) vanishes. The schematics of the configuration in sketched in Fig. 4(a). The effective Rényi reflected entropy of order one half is computed in terms of a correlation function of twist operators σ_{g_A} and σ_{g_B} at the endpoints of the intervals as follows:

$$\begin{aligned} S_{R\,\mathrm{eff}}^{(1/2)}(A:B \cup I_R(B)) &= \lim_{m\to 1}\lim_{n\to\frac{1}{2}} \frac{1}{1-n} \log \frac{\langle \sigma_{g_A}(b_1)\sigma_{g_A^{-1}}(b_2)\sigma_{g_B}(b_3)\sigma_{g_B^{-1}}(-b_3)\rangle_{mn}}{(\langle \sigma_{g_m}(b_1)\sigma_{g_m^{-1}}(b_2)\sigma_{g_m}(b_3)\sigma_{g_m^{-1}}(-b_3)\rangle_m)^n} \\ &\approx \lim_{m\to 1}\lim_{n\to\frac{1}{2}} \frac{1}{1-n} \log \frac{\langle \sigma_{g_A}(b_1)\sigma_{g_A^{-1}}(b_2)\rangle_{mn}\langle \sigma_{g_B}(b_3)\sigma_{g_B^{-1}}(b_4)\rangle_{mn}}{(\langle \sigma_{g_m}(b_1)\sigma_{g_m^{-1}}(b_2)\rangle_m \langle \sigma_{g_m}(b_3)\sigma_{g_m^{-1}}(b_4)\rangle_m)^n} \\ &= 0. \end{aligned} \tag{A3}$$

As a result, the Rényi reflected entropy of order one half and consequently the entanglement negativity is vanishing in this phase. This is consistent with the geometric description of the Markov gap as the bulk entanglement wedge is disconnected.

b. Phase-II

In this phase, A still does not acquire an island while the bulk entanglement wedge is connected and the corresponding wedge cross section lands on the extremal surface of $A \cup B$ [63]. As depicted in Fig. 5(a), in this phase, once again there is no nontrivial reflected island cross section. The effective Rényi reflected entropy of order one half is given by [27,164]

$$S_{R\mathrm{eff}}^{(1/2)}(A:B\cup I_R(B)) = \lim_{m\to 1}\lim_{n\to\frac{1}{2}} \frac{1}{1-n} \log \frac{\langle \sigma_{g_A}(-b_1)\sigma_{g_A^{-1}}(b_1)\sigma_{g_B}(b_2)\sigma_{g_B^{-1}}(b_3)\rangle_{mn}}{(\langle \sigma_{g_m}(-b_1)\sigma_{g_m^{-1}}(b_1)\sigma_{g_m}(b_2)\sigma_{g_m^{-1}}(b_3)\rangle_m)^n}, \tag{A4}$$

where the conformal weights of the twist fields σ_{g_A}, σ_{g_B} and σ_{g_m} are given by

$$h_{g_A} = h_{g_B} = \frac{nc}{24}\left(m - \frac{1}{m}\right), \quad h_{g_m} = \frac{c}{24}\left(m - \frac{1}{m}\right). \tag{A5}$$

The computation is similar to [27,164], and in the proximity limit $b_2 \to b_3$ we obtain

$$S_{R\mathrm{eff}}^{(1/2)}(A:B\cup I_R(B)) = \frac{c}{2}\log\left[\frac{2(b_1+b_2)(b_3-b_1)}{b_1(b_3-b_2)}\right], \tag{A6}$$

and correspondingly the entanglement negativity between A and B, obtained through the alternative proposal in Eq. (2.14), reads

$$\tilde{\mathcal{E}}(A:B) = \frac{c}{4}\log\left[\frac{2(b_1+b_2)(b_3-b_1)}{b_1(b_3-b_2)}\right]. \tag{A7}$$

Note that, the above expression differs from Eq. (4.16) by an additive constant $\frac{c}{4}\log 4 = \frac{3}{2}\frac{\log 4}{4G_N}$, which is reminiscent of the imperfect Markov recovery process. Furthermore, this constant gap is consistent with the geometric interpretation of the Markov gap in terms of the number of nontrivial boundaries of the bulk EWCS.

c. Phase-III

In this phase, we consider A to be large enough to possess its own entanglement island and the bulk entanglement wedge is once again connected. As sketched in Fig. 6, there is a nontrivial island cross section denoted by the point a' and hence the area contribution for the reflected entropy island cross section in Eq. (A1) is given by Eq. (A2). On the other hand, the effective Rényi reflected entropy is given by [27,164]

$$S^{(m,n)}_{R\,\mathrm{eff}}(A\cup I_R(A):B\cup I_R(B)) = \frac{1}{1-n}\log\frac{(\epsilon_y\Omega(-a'))^{2h_{g_A^{-1}g_B}}\langle\sigma_{g_A^{-1}}(-b_1)\sigma_{g_A}(b_1)\sigma_{g_B}(b_2)\sigma_{g_B^{-1}}(b_3)\sigma_{g_A^{-1}g_B}(-a')\rangle_{mn}}{(\langle\sigma_{g_m}(-b_1)\sigma_{g_m^{-1}}(b_1)\sigma_{g_m}(b_2)\sigma_{g_m^{-1}}(b_3)\rangle_m)^n}, \tag{A8}$$

where ϵ_y is a UV regulator on the AdS_2 brane $\mathbb{Q}$ and $\Omega(-a')$ is given in Eq. (4.2). In the above equation, the composite-twist operator $\sigma_{g_A^{-1}g_B}$ gives the dominant contribution to the OPE of $\sigma_{g_A^{-1}}$ and σ_{g_B} and has the conformal dimension

$$h_{g_A^{-1}g_B} = \frac{c}{12}\left(n-\frac{1}{n}\right) \equiv 2h_n. \tag{A9}$$

The correlation functions of the twist operators appearing in Eq. (A8) may be factorized in the respective channel in the large central-charge limit [27,164]. In the replica limit $m\to 1$, $n\to\frac{1}{2}$ we obtain the generalized reflected entropy as

$$S^{(1/2)}_{R\,\mathrm{gen}}(A:B) = \frac{c}{2}\left[\log\frac{2\ell(b_3+a')(b_2+a')}{a'(b_3-b_2)\epsilon_y\cos\theta_0}+\tanh^{-1}(\sin\theta_0)\right]. \tag{A10}$$

Extremizing over the island cross section a', we obtain $a'=\sqrt{b_2b_3}$ and the corresponding Rényi reflected entropy of order one half is given by

$$S^{(1/2)}_{R}(A:B) = \frac{c}{2}\left[\tanh^{-1}(\sin\theta_0)+\log\left(\frac{\sqrt{b_3}+\sqrt{b_2}}{\sqrt{b_3}-\sqrt{b_2}}\right) + \log\left(\frac{2\ell}{\epsilon_y\cos\theta_0}\right)\right]. \tag{A11}$$

The entanglement negativity between A and B in this phase, computed through the alternative proposal in Eq. (2.14), differs from the expression in Eq. (4.31) in the main body by an additive Markov gap $\frac{c}{4}\log 2$ owing to a single nontrivial boundary of the bulk EWCS.

2. Two adjacent intervals

Next we consider the mixed-state configuration of two adjacent intervals $A=[0,b_1]$ and $B=[b_1,b_2]$ in the bath CFT_2 coupled to the gravity theory on the EOW brane $\mathbb{Q}$. Similar to the discussion of the entanglement negativity in Sec. IV B, there are two possible phases for the Rényi reflected entropy which we investigate below.

a. Phase-I

As the interval A is adjacent to the interface of the bath and the brane CFT_2 it always possess an entanglement island. In phase-I, the interval B is large enough to acquire its entanglement island as depicted in Fig. 8. There exists a nontrivial reflected island cross section[18] Γ_R at the point $a=b_1$ and the corresponding area contribution to the generalized Rényi reflected entropy of order one half is given in Eq. (A2). The effective semiclassical Rényi reflected entropy of order one half may be obtained through correlators of twist operators as follows:

$$S^{(1/2)}_{R\,\mathrm{eff}}(A\cup I_R(A):B\cup I_R(B)) = \lim_{m\to1}\lim_{n\to\frac{1}{2}}\frac{1}{1-n}\log\frac{(\epsilon_y\Omega(-a))^{2h_{g_A^{-1}g_B}}\langle\sigma_{g_A^{-1}g_B}(b_1)\sigma_{g_B}(b_2)\sigma_{g_B^{-1}}(-a')\sigma_{g_Bg_{A^{-1}}}(-b_1)\rangle_{mn}}{(\langle\sigma_{g_m}(b_2)\sigma_{g_m}(-a')\rangle_m)^n}. \tag{A12}$$

In the large central-charge limit, the twist correlator in the numerator factorizes in the corresponding OPE channel as follows [27,164]:

$$\langle\sigma_{g_A^{-1}g_B}(b_1)\sigma_{g_B}(b_2)\sigma_{g_B^{-1}}(-a')\sigma_{g_Bg_{A^{-1}}}(-b_1)\rangle_{mn} \approx \langle\sigma_{g_A^{-1}g_B}(b_1)\sigma_{g_Bg_{A^{-1}}}(-b_1)\rangle_{mn}\langle\sigma_{g_B^{-1}}(-a')\sigma_{g_B}(b_2)\rangle_{mn}. \tag{A13}$$

[18]Note that, in this phase the island cross section is determined solely thorough the entanglement entropy computation of the interval A, which fixes its location at $a=b_1$.

After taking the replica limits $m \to 1, n \to \frac{1}{2}$ and adding the area contribution, the total Rényi reflected entropy of order one half may be written as follows:

$$S_R^{(1/2)}(A:B) = \frac{c}{2}\left[\log\left(\frac{2b_1}{\epsilon}\right) + \log\left(\frac{2\ell}{\epsilon_y \cos\theta_0}\right) + \tanh^{-1}(\sin\theta_0)\right]. \tag{A14}$$

The entanglement negativity obtained through the proposal in Eq. (2.14) matches exactly with Eq. (4.33) since there are no nontrivial boundaries of the bulk EWCS and the corresponding Markov gap vanishes.

b. Phase-II

In phase-II, the interval B is so small to possess an entanglement island and correspondingly there is no island cross section of the brane, as depicted in Fig. 9. In this phase, the bulk EWCS ends on the extremal surface for $A \cup B$. The effective semiclassical Rényi reflected entropy of order one half is given by

$$\begin{aligned} S_{R\,\mathrm{eff}}^{(1/2)}(A:B\cup I_R(B)) &= \lim_{m\to 1}\lim_{n\to\frac{1}{2}}\frac{1}{1-n}\log\frac{\langle\sigma_{g_A}(-b_1)\sigma_{g_A^{-1}g_B}(b_1)\sigma_{g_B^{-1}}(b_2)\rangle_{mn}}{(\langle\sigma_{g_m^{-1}}(-b_1)\sigma_{g_m}(b_2)\rangle_m)^n} \\ &= \lim_{m\to 1}\lim_{n\to\frac{1}{2}}\frac{1}{1-n}\log\left[\frac{(2m)^{-4h_n}(2b_1(b_2-b_1))^{-4h_n}(b_1+b_2)^{4h_n-4h_{g_A}}}{(b_1+b_2)^{-4nh_{g_m}}}\right] \\ &= \frac{c}{2}\log\left[\frac{4b_1(b_2-b_1)}{(b_2+b_1)\epsilon}\right], \end{aligned} \tag{A15}$$

where h_n is defined in Eq. (A9) and we have used the usual form of the three-point correlator in the numerator [129]. The entanglement negativity between A and B in this phase may now be obtained through Eq. (2.14) as follows:

$$\tilde{\mathcal{E}}(A:B) = \frac{c}{4}\log\left[\frac{2b_1(b_2-b_1)}{(b_2+b_1)\epsilon}\right] + \frac{c}{4}\log 2. \tag{A16}$$

Note that the above expression involves an additive constant $\frac{c}{4}\log 2$ compared to Eq. (4.37) in the main text. Once again, this constant Markov gap is consistent with the geometric interpretation described in [169].

---

[1] A. Almheiri, R. Mahajan, J. Maldacena, and Y. Zhao, The Page curve of Hawking radiation from semiclassical geometry, J. High Energy Phys. 03 (2020) 149.

[2] A. Almheiri, N. Engelhardt, D. Marolf, and H. Maxfield, The entropy of bulk quantum fields and the entanglement wedge of an evaporating black hole, J. High Energy Phys. 12 (2019) 063.

[3] A. Almheiri, T. Hartman, J. Maldacena, E. Shaghoulian, and A. Tajdini, Replica wormholes and the entropy of Hawking radiation, J. High Energy Phys. 05 (2020) 013.

[4] A. Almheiri, R. Mahajan, and J. E. Santos, Entanglement islands in higher dimensions, SciPost Phys. **9**, 001 (2020).

[5] A. Almheiri, R. Mahajan, and J. Maldacena, Islands outside the horizon, arXiv:1910.11077.

[6] A. Almheiri, T. Hartman, J. Maldacena, E. Shaghoulian, and A. Tajdini, The entropy of Hawking radiation, Rev. Mod. Phys. **93**, 035002 (2021).

[7] D. N. Page, Information in black hole radiation, Phys. Rev. Lett. **71**, 3743 (1993).

[8] D. N. Page, Average entropy of a subsystem, Phys. Rev. Lett. **71**, 1291 (1993).

[9] D. N. Page, Time dependence of Hawking radiation entropy, J. Cosmol. Astropart. Phys. 09 (2013) 028.

[10] S. Ryu and T. Takayanagi, Holographic derivation of entanglement entropy from AdS/CFT, Phys. Rev. Lett. **96**, 181602 (2006).

[11] V. E. Hubeny, M. Rangamani, and T. Takayanagi, A covariant holographic entanglement entropy proposal, J. High Energy Phys. 07 (2007) 062.

[12] T. Faulkner, A. Lewkowycz, and J. Maldacena, Quantum corrections to holographic entanglement entropy, J. High Energy Phys. 11 (2013) 074.

[13] N. Engelhardt and A. C. Wall, Quantum extremal surfaces: Holographic entanglement entropy beyond the classical regime, J. High Energy Phys. 01 (2015) 073.

[14] L. Anderson, O. Parrikar, and R. M. Soni, Islands with gravitating baths: Towards ER = EPR, J. High Energy Phys. 10 (2020) 226.

[15] Y. Chen, Pulling out the island with modular flow, J. High Energy Phys. 03 (2020) 033.
[16] V. Balasubramanian, A. Kar, O. Parrikar, G. Sárosi, and T. Ugajin, Geometric secret sharing in a model of Hawking radiation, J. High Energy Phys. 01 (2021) 177.
[17] Y. Chen, X.-L. Qi, and P. Zhang, Replica wormhole and information retrieval in the SYK model coupled to Majorana chains, J. High Energy Phys. 06 (2020) 121.
[18] F. F. Gautason, L. Schneiderbauer, W. Sybesma, and L. Thorlacius, Page curve for an evaporating black hole, J. High Energy Phys. 05 (**2020**) 091.
[19] A. Bhattacharya, Multipartite purification, multiboundary wormholes, and islands in AdS_3/CFT_2, Phys. Rev. D **102**, 046013 (2020).
[20] T. Anegawa and N. Iizuka, Notes on islands in asymptotically flat 2d dilaton black holes, J. High Energy Phys. 07 (2020) 036.
[21] K. Hashimoto, N. Iizuka, and Y. Matsuo, Islands in Schwarzschild black holes, J. High Energy Phys. 06 (2020) 085.
[22] T. Hartman, E. Shaghoulian, and A. Strominger, Islands in asymptotically flat 2D gravity, J. High Energy Phys. 07 (2020) 022.
[23] C. Krishnan, V. Patil, and J. Pereira, Page curve and the information paradox in flat space, arXiv:2005.02993.
[24] M. Alishahiha, A. Faraji Astaneh, and A. Naseh, Island in the presence of higher derivative terms, J. High Energy Phys. 02 (2021) 035.
[25] H. Geng and A. Karch, Massive islands, J. High Energy Phys. 09 (2020) 121.
[26] T. Li, J. Chu, and Y. Zhou, Reflected entropy for an evaporating black hole, J. High Energy Phys. 11 (2020) 155.
[27] V. Chandrasekaran, M. Miyaji, and P. Rath, Including contributions from entanglement islands to the reflected entropy, Phys. Rev. D **102**, 086009 (2020).
[28] D. Bak, C. Kim, S.-H. Yi, and J. Yoon, Unitarity of entanglement and islands in two-sided Janus black holes, J. High Energy Phys. 01 (**2021**) 155.
[29] C. Krishnan, Critical islands, J. High Energy Phys. 01 (2021) 179.
[30] A. Karlsson, Replica wormhole and island incompatibility with monogamy of entanglement, arXiv:2007.10523.
[31] T. Hartman, Y. Jiang, and E. Shaghoulian, Islands in cosmology, J. High Energy Phys. 11 (2020) 111.
[32] V. Balasubramanian, A. Kar, and T. Ugajin, Entanglement between two disjoint universes, J. High Energy Phys. 02 (2021) 136.
[33] V. Balasubramanian, A. Kar, and T. Ugajin, Islands in de Sitter space, J. High Energy Phys. 02 (2021) 072.
[34] W. Sybesma, Pure de Sitter space and the island moving back in time, Classical Quantum Gravity **38**, 145012 (2021).
[35] H. Z. Chen, R. C. Myers, D. Neuenfeld, I. A. Reyes, and J. Sandor, Quantum extremal islands made easy, part I: Entanglement on the brane, J. High Energy Phys. 10 (2020) 166.
[36] H. Z. Chen, R. C. Myers, D. Neuenfeld, I. A. Reyes, and J. Sandor, Quantum extremal islands made easy, part II: Black holes on the brane, J. High Energy Phys. 12 (2020) 025.
[37] J. Hernandez, R. C. Myers, and S.-M. Ruan, Quantum extremal islands made easy. Part III. Complexity on the brane, J. High Energy Phys. 02 (2021) 173.
[38] G. Grimaldi, J. Hernandez, and R. C. Myers, Quantum extremal islands made easy, part IV: Massive black holes on the brane, J. High Energy Phys. 03 (2022) 136.
[39] Y. Ling, Y. Liu, and Z.-Y. Xian, Island in charged black holes, J. High Energy Phys. 03 (2021) 251.
[40] D. Marolf and H. Maxfield, Observations of Hawking radiation: The Page curve and baby universes, J. High Energy Phys. 04 (2021) 272.
[41] Y. Matsuo, Islands and stretched horizon, J. High Energy Phys. 07 (2021) 051.
[42] I. Akal, Y. Kusuki, N. Shiba, T. Takayanagi, and Z. Wei, Entanglement entropy in a holographic moving mirror and the Page curve, Phys. Rev. Lett. **126**, 061604 (2021).
[43] E. Caceres, A. Kundu, A. K. Patra, and S. Shashi, Warped information and entanglement islands in AdS/WCFT, J. High Energy Phys. 07 (**2021**) 004.
[44] S. Raju, Lessons from the information paradox, Phys. Rep. **943**, 1 (2022).
[45] F. Deng, J. Chu, and Y. Zhou, Defect extremal surface as the holographic counterpart of Island formula, J. High Energy Phys. 03 (2021) 008.
[46] T. Anous, M. Meineri, P. Pelliconi, and J. Sonner, Sailing past the End of the World and discovering the Island, SciPost Phys. **13**, 075 (2022).
[47] R. Bousso and E. Wildenhain, Islands in closed and open universes, Phys. Rev. D **105**, 086012 (2022).
[48] Q.-L. Hu, D. Li, R.-X. Miao, and Y.-Q. Zeng, AdS/BCFT and Island for curvature-squared gravity, J. High Energy Phys. 09 (2022) 037.
[49] C. Akers, T. Faulkner, S. Lin, and P. Rath, The Page curve for reflected entropy, J. High Energy Phys. 06 (2022) 089.
[50] M.-H. Yu, C.-Y. Lu, X.-H. Ge, and S.-J. Sin, Island, Page curve and superradiance of rotating BTZ black holes, Phys. Rev. D **105**, 066009 (2022).
[51] S. Fallows and S. F. Ross, Islands and mixed states in closed universes, J. High Energy Phys. 07 (2021) 022.
[52] H. Geng, A. Karch, C. Perez-Pardavila, S. Raju, L. Randall, M. Riojas, and S. Shashi, Entanglement phase structure of a holographic BCFT in a black hole background, J. High Energy Phys. 05 (2022) 153.
[53] C.-J. Chou, H. B. Lao, and Y. Yang, Page curve of effective Hawking radiation, Phys. Rev. D **106**, 066008 (2022).
[54] T. J. Hollowood, S. P. Kumar, A. Legramandi, and N. Talwar, Grey-body factors, irreversibility and multiple island saddles, J. High Energy Phys. 03 (2022) 110.
[55] S. He, Y. Sun, L. Zhao, and Y.-X. Zhang, The universality of islands outside the horizon, J. High Energy Phys. 05 (2022) 047.
[56] I. Aref'eva and I. Volovich, A note on islands in Schwarzschild black holes, Teor. Mat. Fiz. **214**, 500 (2023).
[57] Y. Ling, P. Liu, Y. Liu, C. Niu, Z.-Y. Xian, and C.-Y. Zhang, Reflected entropy in double holography, J. High Energy Phys. 02 (2022) 037.
[58] A. Bhattacharya, A. Bhattacharyya, P. Nandy, and A. K. Patra, Partial islands and subregion complexity in geometric secret-sharing model, J. High Energy Phys. 12 (2021) 091.

[59] S. Azarnia, R. Fareghbal, A. Naseh, and H. Zolfi, Islands in flat-space cosmology, Phys. Rev. D **104**, 126017 (2021).
[60] A. Saha, S. Gangopadhyay, and J. P. Saha, Mutual information, islands in black holes and the Page curve, Eur. Phys. J. C **82**, 476 (2022).
[61] T. J. Hollowood, S. P. Kumar, A. Legramandi, and N. Talwar, Ephemeral islands, plunging quantum extremal surfaces and BCFT channels, J. High Energy Phys. 01 (2022) 078.
[62] P.-C. Sun, Entanglement islands from holographic thermalization of rotating charged black hole, arXiv:2108.12557.
[63] T. Li, M.-K. Yuan, and Y. Zhou, Defect extremal surface for reflected entropy, J. High Energy Phys. 01 (2022) 018.
[64] S. E. Aguilar-Gutierrez, A. Chatwin-Davies, T. Hertog, N. Pinzani-Fokeeva, and B. Robinson, Islands in multiverse models, J. High Energy Phys. 11 (2021) 212.
[65] B. Ahn, S.-E. Bak, H.-S. Jeong, K.-Y. Kim, and Y.-W. Sun, Islands in charged linear dilaton black holes, Phys. Rev. D **105**, 046012 (2022).
[66] M.-H. Yu and X.-H. Ge, Islands and Page curves in charged dilaton black holes, Eur. Phys. J. C **82**, 14 (2022).
[67] Y. Lu and J. Lin, Islands in Kaluza–Klein black holes, Eur. Phys. J. C **82**, 132 (2022).
[68] E. Caceres, A. Kundu, A. K. Patra, and S. Shashi, Page curves and bath deformations, SciPost Phys. Core **5**, 033 (2022).
[69] I. Akal, Y. Kusuki, N. Shiba, T. Takayanagi, and Z. Wei, Holographic moving mirrors, Classical Quantum Gravity **38**, 224001 (2021).
[70] I. Aref'eva, T. Rusalev, and I. Volovich, Entanglement entropy of near-extremal black hole, Teor. Mat. Fiz. **212**, 457 (2022).
[71] I. Aref'eva and I. Volovich, Complete evaporation of black holes and Page curves, Symmetry **15**, 170 (2023).
[72] R. Bousso, X. Dong, N. Engelhardt, T. Faulkner, T. Hartman, S.H. Shenker, and D. Stanford, Snowmass White Paper: Quantum aspects of black holes and the emergence of spacetime, arXiv:2201.03096.
[73] C. Krishnan and V. Mohan, Interpreting the bulk Page curve: A vestige of locality on holographic screens, arXiv:2112.13783.
[74] D.-f. Zeng, Spontaneous radiation of black holes, Nucl. Phys. **B977**, 115722 (2022).
[75] D. Teresi, Islands and the de Sitter entropy bound, J. High Energy Phys. 10 (2022) 179.
[76] K. Okuyama and K. Sakai, Page curve from dynamical branes in JT gravity, J. High Energy Phys. 02 (2022) 087.
[77] P. Chen, M. Sasaki, D.-h. Yeom, and J. Yoon, Solving information loss paradox via Euclidean path integral, arXiv:2111.01005.
[78] J. F. Pedraza, A. Svesko, W. Sybesma, and M. R. Visser, Microcanonical action and the entropy of Hawking radiation, Phys. Rev. D **105**, 126010 (2022).
[79] B. Guo, M. R. R. Hughes, S. D. Mathur, and M. Mehta, Contrasting the fuzzball and wormhole paradigms for black holes, Turk. J. Phys. **45**, 281 (2021).
[80] T. Kibe, P. Mandayam, and A. Mukhopadhyay, Holographic spacetime, black holes and quantum error correcting codes: A review, Eur. Phys. J. C **82**, 463 (2022).
[81] R. Renner and J. Wang, The black hole information puzzle and the quantum de Finetti theorem, arXiv:2110.14653.
[82] X. Dong, S. McBride, and W. W. Weng, Replica wormholes and holographic entanglement negativity, J. High Energy Phys. 06 (2022) 094.
[83] S. Raju, Failure of the split property in gravity and the information paradox, Classical Quantum Gravity **39**, 064002 (2022).
[84] C. H. Nam, Entanglement entropy and Page curve of black holes with island in massive gravity, Eur. Phys. J. C **82**, 381 (2022).
[85] J. Kames-King, E. Verheijden, and E. Verlinde, No Page curves for the de Sitter horizon, J. High Energy Phys. 03 (2022) 040.
[86] B. Chen, B. Czech, and Z.-z. Wang, Quantum information in holographic duality, Rep. Prog. Phys. **85**, 046001 (2022).
[87] Y. Sato, Complexity in a moving mirror model, Phys. Rev. D **105**, 086016 (2022).
[88] J. Kudler-Flam, V. Narovlansky, and S. Ryu, Distinguishing random and black hole microstates, PRX Quantum **2**, 040340 (2021).
[89] X. Wang, K. Zhang, and J. Wang, What can we learn about islands and state paradox from quantum information theory?, arXiv:2107.09228.
[90] D. S. Ageev, Shaping contours of entanglement islands in BCFT, J. High Energy Phys. 03 (2022) 033.
[91] L. Buoninfante, F. Di Filippo, and S. Mukohyama, On the assumptions leading to the information loss paradox, J. High Energy Phys. 10 (**2021**) 081.
[92] M. Cadoni and A. P. Sanna, Unitarity and Page curve for evaporation of 2D AdS black holes, arXiv:2106.14738.
[93] D. Marolf and H. Maxfield, The Page curve and baby universes, Int. J. Mod. Phys. D **30**, 2142027 (2021).
[94] J. Chu, F. Deng, and Y. Zhou, Page curve from defect extremal surface and island in higher dimensions, J. High Energy Phys. 10 (2021) 149.
[95] E. Y. Urbach, The entanglement entropy of typical pure states and replica wormholes, J. High Energy Phys. 12 (2021) 125.
[96] R. Li, X. Wang, and J. Wang, Island may not save the information paradox of Liouville black holes, Phys. Rev. D **104**, 106015 (2021).
[97] D. Neuenfeld, Homology conditions for RT surfaces in double holography, Classical Quantum Gravity **39**, 075009 (2022).
[98] L. Aalsma and W. Sybesma, The price of curiosity: Information recovery in de Sitter space, J. High Energy Phys. 05 (2021) 291.
[99] K. Ghosh and C. Krishnan, Dirichlet baths and the not-so-fine-grained Page curve, J. High Energy Phys. 08 (2021) 119.
[100] A. Bhattacharya, A. Bhattacharyya, P. Nandy, and A. K. Patra, Islands and complexity of eternal black hole and radiation subsystems for a doubly holographic model, J. High Energy Phys. 05 (2021) 135.
[101] H. Geng, Y. Nomura, and H.-Y. Sun, Information paradox and its resolution in de Sitter holography, Phys. Rev. D **103**, 126004 (2021).

[102] C. Krishnan and V. Mohan, Hints of gravitational ergodicity: Berry's ensemble and the universality of the semi-classical Page curve, J. High Energy Phys. 05 (2021) 126.
[103] E. Verheijden and E. Verlinde, From the BTZ black hole to JT gravity: Geometrizing the island, J. High Energy Phys. 11 (2021) 092.
[104] R. Bousso and A. Shahbazi-Moghaddam, Island finder and entropy bound, Phys. Rev. D **103**, 106005 (2021).
[105] G. K. Karananas, A. Kehagias, and J. Taskas, Islands in linear dilaton black holes, J. High Energy Phys. 03 (2021) 253.
[106] K. Goto, T. Hartman, and A. Tajdini, Replica wormholes for an evaporating 2D black hole, J. High Energy Phys. 04 (2021) 289.
[107] A. Bhattacharya, A. Chanda, S. Maulik, C. Northe, and S. Roy, Topological shadows and complexity of islands in multiboundary wormholes, J. High Energy Phys. 02 (2021) 152.
[108] H. Z. Chen, Z. Fisher, J. Hernandez, R. C. Myers, and S.-M. Ruan, Evaporating black holes coupled to a thermal bath, J. High Energy Phys. 01 (2021) 065.
[109] C. A. Agón, S. F. Lokhande, and J. F. Pedraza, Local quenches, bulk entanglement entropy and a unitary Page curve, J. High Energy Phys. 08 (2020) 152.
[110] A. Laddha, S. G. Prabhu, S. Raju, and P. Shrivastava, The holographic nature of null infinity, SciPost Phys. **10**, 041 (2021).
[111] C. Akers, N. Engelhardt, and D. Harlow, Simple holographic models of black hole evaporation, J. High Energy Phys. 08 (2020) 032.
[112] H. Z. Chen, Z. Fisher, J. Hernandez, R. C. Myers, and S.-M. Ruan, Information flow in black hole evaporation, J. High Energy Phys. 03 (**2020**) 152.
[113] J. K. Basak, D. Basu, V. Malvimat, H. Parihar, and G. Sengupta, Reflected entropy and entanglement negativity for holographic moving mirrors, J. High Energy Phys. 09 (2022) 089.
[114] H. Geng, A. Karch, C. Perez-Pardavila, S. Raju, L. Randall, M. Riojas, and S. Shashi, Information transfer with a gravitating bath, SciPost Phys. **10**, 103 (2021).
[115] H. Geng, S. Lüst, R. K. Mishra, and D. Wakeham, Holographic BCFTs and communicating black holes, J. High Energy Phys. 08 (2021) 003.
[116] M. Afrasiar, J. Kumar Basak, A. Chandra, and G. Sengupta, Islands for entanglement negativity in communicating black holes, Phys. Rev. D **108**, 066013 (2023).
[117] G. Yadav, Page curves of Reissner-Nordström black hole in HD gravity, Eur. Phys. J. C **82**, 904 (2022).
[118] C. F. Uhlemann, Information transfer with a twist, J. High Energy Phys. 01 (2022) 126.
[119] C. F. Uhlemann, Islands and Page curves in 4d from Type IIB, J. High Energy Phys. 08 (2021) 104.
[120] C. Germani, Retrieving black hole information from the main Lorentzian saddle point, Phys. Rev. D **106**, 066018 (2022).
[121] F. Omidi, Entropy of Hawking radiation for two-sided hyperscaling violating black branes, J. High Energy Phys. 04 (2022) 022.
[122] J. Maldacena and L. Susskind, Cool horizons for entangled black holes, Fortschr. Phys. **61**, 781 (2013).
[123] J. L. Cardy, Boundary conformal field theory, *Encyclopedia of Mathematical Physics* (Elsevier, New York, 2006).
[124] T. Takayanagi, Holographic dual of BCFT, Phys. Rev. Lett. **107**, 101602 (2011).
[125] M. Fujita, T. Takayanagi, and E. Tonni, Aspects of AdS/BCFT, J. High Energy Phys. 11 (2011) 043.
[126] M. Rozali, J. Sully, M. Van Raamsdonk, C. Waddell, and D. Wakeham, Information radiation in BCFT models of black holes, J. High Energy Phys. 05 (2020) 004.
[127] J. Sully, M. V. Raamsdonk, and D. Wakeham, BCFT entanglement entropy at large central charge and the black hole interior, J. High Energy Phys. 03 (2021) 167.
[128] J. Kastikainen and S. Shashi, Structure of holographic BCFT correlators from geodesics, Phys. Rev. D **105**, 046007 (2022).
[129] S. Dutta and T. Faulkner, A canonical purification for the entanglement wedge cross-section, J. High Energy Phys. 03 (2021) 178.
[130] C. Akers, T. Faulkner, S. Lin, and P. Rath, Reflected entropy in random tensor networks, J. High Energy Phys. 05 (2022) 162.
[131] G. Vidal and R. F. Werner, Computable measure of entanglement, Phys. Rev. A **65**, 032314 (2002).
[132] M. B. Plenio, Logarithmic negativity: A full entanglement monotone that is not convex, Phys. Rev. Lett. **95**, 090503 (2005).
[133] T. Takayanagi and K. Umemoto, Entanglement of purification through holographic duality, Nat. Phys. **14**, 573 (2018).
[134] P. Nguyen, T. Devakul, M. G. Halbasch, M. P. Zaletel, and B. Swingle, Entanglement of purification: From spin chains to holography, J. High Energy Phys. 01 (2018) 098.
[135] Q. Wen, Balanced partial entanglement and the entanglement wedge cross section, J. High Energy Phys. 04 (2021) 301.
[136] H. A. Camargo, P. Nandy, Q. Wen, and H. Zhong, Balanced partial entanglement and mixed state correlations, SciPost Phys. **12**, 137 (2022).
[137] P. Calabrese, J. Cardy, and E. Tonni, Entanglement negativity in quantum field theory, Phys. Rev. Lett. **109**, 130502 (2012).
[138] P. Calabrese, J. Cardy, and E. Tonni, Entanglement negativity in extended systems: A field theoretical approach, J. Stat. Mech. (2013) P02008.
[139] P. Calabrese, J. Cardy, and E. Tonni, Finite temperature entanglement negativity in conformal field theory, J. Phys. A **48**, 015006 (2015).
[140] V. Malvimat, H. Parihar, B. Paul, and G. Sengupta, Entanglement negativity in Galilean conformal field theories, Phys. Rev. D **100**, 026001 (2019).
[141] D. Basu, A. Chandra, H. Parihar, and G. Sengupta, Entanglement negativity in flat holography, SciPost Phys. **12**, 074 (2022).
[142] M. R. Setare and M. Koohgard, Holographic entanglement negativity in flat space generalized minimal massive gravity, Int. J. Mod. Phys. A **37**, 2250024 (2022).
[143] M. Rangamani and M. Rota, Comments on entanglement negativity in holographic field theories, J. High Energy Phys. 10 (2014) 060.

[144] P. Chaturvedi, V. Malvimat, and G. Sengupta, Entanglement negativity, holography and black holes, Eur. Phys. J. C **78**, 499 (2018).
[145] P. Chaturvedi, V. Malvimat, and G. Sengupta, Holographic quantum entanglement negativity, J. High Energy Phys. 05 (2018) 172.
[146] P. Jain, V. Malvimat, S. Mondal, and G. Sengupta, Holographic entanglement negativity conjecture for adjacent intervals in AdS_3/CFT_2, Phys. Lett. B **793**, 104 (2019).
[147] P. Jain, V. Malvimat, S. Mondal, and G. Sengupta, Holographic entanglement negativity for adjacent subsystems in AdS_{d+1}/CFT_d, Eur. Phys. J. Plus **133**, 300 (2018).
[148] P. Chaturvedi, V. Malvimat, and G. Sengupta, Covariant holographic entanglement negativity, Eur. Phys. J. C **78**, 776 (2018).
[149] P. Jain, V. Malvimat, S. Mondal, and G. Sengupta, Covariant holographic entanglement negativity for adjacent subsystems in AdS_3/CFT_2, Nucl. Phys. **B945**, 114683 (2019).
[150] P. Jain, V. Malvimat, S. Mondal, and G. Sengupta, Holographic entanglement negativity for conformal field theories with a conserved charge, Eur. Phys. J. C **78**, 908 (2018).
[151] V. Malvimat, S. Mondal, B. Paul, and G. Sengupta, Holographic entanglement negativity for disjoint intervals in AdS_3/CFT_2, Eur. Phys. J. C **79**, 191 (2019).
[152] V. Malvimat, S. Mondal, B. Paul, and G. Sengupta, Covariant holographic entanglement negativity for disjoint intervals in AdS_3/CFT_2, Eur. Phys. J. C **79**, 514 (2019).
[153] J. Kumar Basak, H. Parihar, B. Paul, and G. Sengupta, Holographic entanglement negativity for disjoint subsystems in AdS_{d+1}/CFT_d, arXiv:2001.10534.
[154] S. Mondal, B. Paul, G. Sengupta, and P. Sharma, Holographic entanglement negativity for a single subsystem in conformal field theories with a conserved charge, arXiv: 2102.05848.
[155] M. Afrasiar, J. K. Basak, V. Raj, and G. Sengupta, Holographic entanglement negativity for disjoint subsystems in conformal field theories with a conserved charge, arXiv: 2106.14918.
[156] D. Basu, H. Parihar, V. Raj, and G. Sengupta, Entanglement negativity, reflected entropy, and anomalous gravitation, Phys. Rev. D **105**, 086013 (2022).
[157] M. Kulaxizi, A. Parnachev, and G. Policastro, Conformal blocks and negativity at large central charge, J. High Energy Phys. 09 (2014) 010.
[158] V. Malvimat and G. Sengupta, Entanglement negativity at large central charge, Phys. Rev. D **103**, 106003 (2021).
[159] J. Kudler-Flam and S. Ryu, Entanglement negativity and minimal entanglement wedge cross sections in holographic theories, Phys. Rev. D **99**, 106014 (2019).
[160] Y. Kusuki, J. Kudler-Flam, and S. Ryu, Derivation of holographic negativity in AdS_3/CFT_2, Phys. Rev. Lett. **123**, 131603 (2019).
[161] J. Kumar Basak, V. Malvimat, H. Parihar, B. Paul, and G. Sengupta, On minimal entanglement wedge cross section for holographic entanglement negativity, arXiv:2002.10272.
[162] J. Kumar Basak, H. Parihar, B. Paul, and G. Sengupta, Covariant holographic negativity from the entanglement wedge in AdS_3/CFT_2, Phys. Lett. B **834**, 137451 (2022).
[163] D. Basu, A. Chandra, V. Raj, and G. Sengupta, Entanglement wedge in flat holography and entanglement negativity, SciPost Phys. Core **5**, 013 (2022).
[164] J. Kumar Basak, D. Basu, V. Malvimat, H. Parihar, and G. Sengupta, Islands for entanglement negativity, SciPost Phys. **12**, 003 (2022).
[165] J. Kumar Basak, D. Basu, V. Malvimat, H. Parihar, and G. Sengupta, Page curve for entanglement negativity through geometric evaporation, SciPost Phys. **12**, 004 (2022).
[166] A. Karch and L. Randall, Locally localized gravity, J. High Energy Phys. 05 (2001) 008.
[167] L. Randall and R. Sundrum, An alternative to compactification, Phys. Rev. Lett. **83**, 4690 (1999).
[168] J. M. Maldacena, The large N limit of superconformal field theories and supergravity, Adv. Theor. Math. Phys. **2**, 231 (1998).
[169] P. Hayden, O. Parrikar, and J. Sorce, The Markov gap for geometric reflected entropy, J. High Energy Phys. 10 (2021) 047.
[170] J. D. Brown and M. Henneaux, Central charges in the canonical realization of asymptotic symmetries: An example from three-dimensional gravity, Commun. Math. Phys. **104**, 207 (1986).